

Droplet Electro-Bouncing in Low-Gravity

by

Erin Stivers Schmidt

A thesis submitted in partial fulfillment of the
requirements for the degree of

Master of Science
in
Mechanical Engineering

Thesis Committee:
Mark Weislogel, Chair
Raúl Bayoán Cal
Gerry Recktenwald

Portland State University
2018

Abstract

We investigate the dynamics of spontaneous jumps of water droplets from electrically charged superhydrophobic dielectric surfaces during a sudden step reduction in gravity level. In the brief free-fall environment of a drop tower, with a non-homogeneous external electric field (with strengths 0.39-2.36 kV/cm) arising due to dielectric surface charges, body forces acting on the jumped droplets are primarily supplied by polarization stress and Coulombic attraction instead of gravity. This electric body force leads to a droplet bouncing behavior similar to well-known phenomena in 1-g, though occurring for much larger droplets (~ 0.5 mL). We show a simple model for the phenomenon, its scaling, and asymptotic estimates for droplet time of flight. The droplet net charge, estimated to be on the order of 1×10^{-9} C, is field induced rather than by contact charging at the (PTFE coated) hydrophobic interface. In 1-g, for Weber numbers > 0.4 , impact recoil behavior on a super-hydrophobic surface is normally dominated by damping from contact line hysteresis. However, at the low Bond and Ohnesorge numbers occurring in free-fall, the droplet impact dynamics additionally include electrohydrodynamic surface wettability effects. This is qualitatively discussed in terms of trends in coefficients of restitution and dimensionless contact time.

To Mom, Laura, and the DDT team.

Acknowledgements

This work was supported by NASA Cooperative Agreement NNX12A047A. I am also greatly indebted to Andrew Greenberg for his frequent and sage technical advice, and to Joe Shields for his assistance with drop tower experiments.

Contents

Abstract	i
Acknowledgements	iii
1 Introduction	1
1.1 Spontaneous Droplet Jump	5
1.2 Droplet Electro-Bounce	6
1.3 Applications	11
1.4 Overview of this Thesis	12
2 Theory	14
2.1 Forces and the Equation of Motion	14
2.2 The Electric Field	20
2.3 Scaling	23
2.3.1 Inertial Electro-Image Limit	24
2.3.2 Inertial Electro-Viscous Limit	25
2.4 Asymptotic Estimates	26
2.4.1 Inertial Electro-Image Limit	26
2.4.2 Inertial Electro-Viscous Limit	28

3 Methodology	33
3.1 Overview	33
3.2 Experimental Methods	34
3.3 Data Munging	44
3.4 Parameter Estimation	45
3.4.1 Inverse Problems	47
3.4.2 Smoothing	49
3.4.3 Optimization	55
3.4.4 Identifiability	59
4 Results	65
4.1 Charge Estimates	65
4.2 Scale Quantities	68
4.3 Impact Dynamics [placeholder section]	72

Appendices

A Parallel Plate Method	78
--------------------------------	-----------

List of Figures

1.1	The trajectory of a 0.5 mL droplet is captured in a composite image over a single bounce period (~ 1.25 s). The surface potential of the superhydrophobic dielectric in this example is $\varphi_s = 1.25 \pm 0.41$ kV.	7
2.1	A log-log plot of the magnitude of the non-dimensional electric field, E_y .	23
2.2	Non-dimensional droplet trajectories for various values of $\mathbb{E}u = \epsilon$, $\mathbb{I}m = \alpha$. The trajectory reduces to the classical $\mathcal{O}(1)$ solution for small values of α . It should be noted that despite what is implied by these plots α is not necessarily completely independent of ϵ , as they share q , and E_0 as common factors, $U_0 \sim R_d^2$, and $m \sim R_d^3$.	28
2.3	Non-dimensional droplet trajectories for various values of $\mathbb{E}u = \epsilon$.	29
2.4	$\mathcal{O}(\epsilon^3)$ asymptotic estimate of droplet time-of-flight as a function of $\epsilon = \mathbb{E}u_+$.	31

3.1	A schematic representation of the droplet initial condition, resting on the superhydrophobic surface in the Cassie-Baxter state just prior to the drop tower experiment. The variables q , σ , and V_d are the droplet net free charge, dielectric surface charge density, and droplet volume respectively.	35
3.2	A schematic representation of a droplet electro-bounce experiment with labeled characteristic time and length scales, t_c , y_c shown. Also shown are the dimensions of the superhydrophobic electret substrate.	36
3.3	The droplet electro-bounce experiment hardware mounted on a drop tower rig.	39
3.4	Hysteresis of the contact line plotted as a function of static contact angle and roll-off angle for 1 mL droplets.	40
3.5	SEM image of the superhydrophobic surface.	41
3.6	Charge decay in the dielectric laminates for differing numbers of layers.	44
3.7	The underlying signal is ‘noisy’, due partially to deterministic errors in determining the center of mass position. These deterministic errors are largely due to droplet oscillations, especially the rapidly damped higher harmonics which do not have azimuthal symmetry. There is also Gaussian error in the ellipse fitting due to thresholding and noise in the video itself. We see that 1D Gaussian convolution and Wiener filters suffer from significant end effects. At this scale Butterworth and Savitsky-Golay filters are nearly indistinguishable.	51

3.8 Comparing the first derivatives of the Butterworth and Savitsky-Golay filters we see that the Butterworth filter also suffers from a slight end effect. This implies that the optimization will find a different optima of the likelyhood depending on which type of filter is used.	52
3.9 The power spectra has a peak at 1 Hz, which is the droplet trajectory parabola itself, and smaller peaks in the kHz range corresponding to various noise frequencies. The Savitsky-Golay and Butterworth filters seem to have the least distortion of the power spectra of the true signal. Both also do a good job of attenuating the noise at the 2 kHz peak.	53
3.10 As is typical with <i>Nelder-Mead</i> much of the improvement in χ^2 is realized in the first few iterations. Overall the rate of convergence is sub-linear, which is to be expected for non-linear constrained problems using an hueristic algorithem. . .	59
3.11 A series of filtered droplet trajectories arranged by increasing apoapse. The blue dots represent either the beginning and end of the experiment, or points at which the droplet is either coming into, or leaving contact with the surface.	60
3.12 A series of droplet trajectories showing the results of the parameter estimation. The trajectories are shown only up to the apoapse of the first bounce. The red lines show the ODE solution with given the MLE parameter vector. χ^2 goodness-of-fit varies between 1×10^{-5} and 1×10^{-8} with the better fit occurring typically for the droplets with the lowest apoapses. .	61

LIST OF FIGURES ix

4.1	A simple EMA plot.	66
4.2	A simple EMA plot.	67
4.3	Droplet trajectories as a function of $\mathbb{E}u$	69
4.4	Simulated forces acting on the droplet. Experiments are shown by order of increasing apoapse.	70
4.5	Non-dimensional trajectories with the short-time scaling. . . .	71
4.6	72
4.7	73
4.8	Non-dimensional trajectories with the long-time scaling as a function of $\mathbb{E}u_+$	74
4.9	75
4.10	76

Chapter 1

Introduction

“When the influence of gravity on fluid behavior is diminished or removed, other forces, otherwise of small significance, can assume paramount roles.” - NRC Report to NASA, 2003 [1]

Our terrestrially born intuition about how liquids flow is easily confounded in a low-gravity environment. This should come as little surprise, as we are creatures evolved at the bottom of a gravity well; gravity is natural to us. However when the magnitude of gravitational body forces become small, other forces come into play in fluid dynamical problems which are otherwise negligible under normal circumstances in 1-g. Our 1-g cognitive bias then leads to a plethora of problems which are both simultaneously trivially easy to solve in 1-g, and which despite decades of study continue to elude solutions in a low-gravity context. One example of these problems is the so-called “phase separation” problem of separating a gas phase from a multi-phase flow (or the reverse case), without the aid of buoyancy due to gravity. Sans buoyancy otherwise mundane activities such as venting a gas or settling a liquid

in a tank become problematic [2]. Trapped bubbles can vapor lock ECLSS (Environmental Control and Life Support), power, or propulsion systems [3]. Issues of phase separation have so bedeviled human endeavors in space that an entire Apollo Saturn 1B mission (AS-203) was earmarked to study them [4]. This problem has for some time motivated a quest for substitute body forces, and the present work follows in that well-worn tradition.

A solid beginning to rectifying our problem of poor low-gravity intuition, would be to quantify how wrong our intuition is. First, let's clear up a common misnomer about the state of "zero-gravity". The theory of general relativity is based on a fundamental equivalence of gravity and acceleration. By measuring acceleration alone, one cannot determine whether one is in gravity-free space or free-falling in a gravitational field (or conversely whether or not one is uniformly accelerating, or standing at rest in a gravitational field). This is sometimes called the equivalence principle of general relativity (e.g. the equivalence of gravitational and inertial mass). In theoretical terms a zero-g experiment performed in a drop tower on the surface of the Earth is equivalent to the same experiment performed in the nearly gravity-free deep space between galaxies, despite the fact that the drop tower itself is enveloped in a 1-g gravity field. At the orbital altitude of the International Space Station (ISS) the gravity level is still nearly 90% of its value at sea-level on Earth, but the astronauts aboard ISS feel weightlessness because they are in free-fall. In a practical sense true zero-g does not exist anywhere in the universe as there are always small, but nonetheless, measurable forces which can accelerate any massive body. For instance in low-Earth orbit, accelerations due to aerodynamic resistance in the tenuous outer atmosphere

are on the order of 1×10^{-6} g (from hence comes the term “microgravity”). This small drag acceleration provides some ersatz gravity, but there are also other forces present. Foremost of these are capillary forces.

Capillary forces are due to the cumulative effects of a large number of very short range molecular interactions and in a 1-g context are usually quite weak, relatively speaking. However, in a low-gravity environment other forces are so weak that the capillary forces becomes extraordinarily strong in a relative sense. In comparing the relative magnitudes of gravity and the capillary force we arrive at our figure of merit for assessing how wrong our fluid mechanical intuition is likely to be in a low-gravity context. This figure of merit is the Bond number dimensionless group

$$\text{Bo} \equiv \frac{gR^2\Delta\rho}{\gamma}$$

where g is the acceleration, R is the interfacial radius of curvature, $\Delta\rho$ is the difference in densities across the interface (which simplifies to ρ , for large $\Delta\rho$, as in the case of a air-water interface), and where γ is the surface tension. In cases where Bo is small, a liquid is effectively in low-gravity regardless of the nominal local gravity level. Very small droplets ($R < 1$ mm), for instance, are in low-gravity for all intents and purposes and have nearly spherical shapes. Contrarily, for cases of large R in a space environment, such as with large diameter spacecraft propellant tanks then $\text{Bo} \gg 1$ even though the acceleration remains small. This is actually a quite useful result, for on the basis of dimensional similarity, it is possible to accurately simulate low-gravity fluid mechanics (say of large propellant tanks), even in small drop

towers simply by scaling dimensionless groups like the Bond number.

As with capillary forces, electrostatic forces have a multitude of applications as substitutes for gravity. Electrohydrodynamic (EHD) body forces have been suggested to combat thermal stratification of propellants under low-g conditions where buoyancy induced natural convection is very small [5]. In this case electro-convection is an analog of natural convection due to a fluid temperature dependent dielectric permitivity gradient (as opposed to a fluid density gradient), in the presence of a body force field (in this case an electric field). The study also suggested applications in cryogenic tank vent screening, and in reducing heat transfer to cryogenic propellants (and thus boiloff losses) by dielectrophoretically positioning ullage vapors around the tank walls as a thermal barrier. EHD forces have been studied for enhancing boiling heat transfer by promotion of bubble detachment and prevention of dryout, again as an ersatz buoyancy [6] [7] [8]. EHD heat pipes, which substitute an electrode structure for the capillary wicking structure of a conventional thermocapillary heat pipe can evade the wicking limit [9]. These are restricted to the use of insulating dielectric liquids (which usually have relatively low thermal conductivity), but are highly robust against dryout, support active flow control, and have low viscous losses. Dielectrophoretic settling of cryogenic propellants (in both total and partial communication PMD configurations), has been studied analytically in both static [10] and dynamic cases [11], and in drop tower experiments [12]. EHD forces have also beeen applied to the low-g slosh baffling problem [13] [14] [15], and studied extensively for the mitigation of vapor pullthrough during tank draining (and concomittent minimization of propellant residuals at burnout) in a series of

experiments at the NASA Lewis (now Glenn) Research Center 2.2 s drop tower facility [16].

1.1 Spontaneous Droplet Jump

Low-gravity phase separation, droplet dynamics, and the dynamics and applications of the so-called spontaneous droplet jump, is an active area of study at the Portland State University Dryen Drop Tower laboratory (DDT). When a nonwetting, gravity dominated sessile droplet (e.g. a puddle), which is initially at rest on a surface in the Cassie-Baxter state suddenly undergoes a large step reduction in $\Delta\theta$ it will spontaneously jump away from the surface. The Cassie-Baxter state, sometimes also known as the Fakir state, is a metastable heterogeneously non-wetting state on a textured surface characterized by the existence of a vapor-layer which separates roughness features of the surface from the bottom of the droplet. The spontaneous droplet jump was first observed experimentally in the Soviet Union by Kirko *et al.* [17] in 1970, and later by Wollman *et al.* in 2016 in a set of experiments conducted using a low-gravity drop tower [18]. The kinetic energy of the jump is supplied by the defect in free surface energy as the new minimum energy surface equilibrium has approximately constant curvature. If the viscous energy losses by shear, and internal flows during roll up are neglected, as well as energy lost due to the hysteresis of the dynamic contact line, then the available kinetic energy is given by

$$KE = SE_2 - SE_1 = [(\sigma A)_{gl} + (\sigma A)_{sg}]_2 - [(\sigma A)_{ls} + (\sigma A)_{gl} + (\sigma A)_{sg}]_1,$$

where the subscripts ₁ and ₂ denote the initial 1-g, and low-g surface energies. The motive force is due to the inertia of internal flows which occur as the interface deflects under the suddenly lessened Bo . The droplet ‘rolls up’ as it jumps away from the surface due to radial motion of a capillary wave away from the contact line. The characteristic time scale of the rolling up scales as $t_j \sim R_p/U (\rho H R_p^2/\sigma)^{1/2}$ [19], which resembles the contact time, $\tau \approx 2.6(\rho R_d^3/\sigma)^{1/2}$ presented by Richard *et al.* in 2002 for the related problem of droplets impacting hydrophobic surfaces in 1-g [20]. For droplets with radial symmetry and sufficiently high initial Bo these waves coalesce as a shock, leading to geysering and creation of satellite drops by the Rayleigh-Plateau breakup of the geyser. In the case of smaller jumping droplets the capillary waves are gradually damped viscously.

The physics of these relatively massive droplets (far beyond the 1-g millimetric capillary length scale) at once utterly defy terrestrial expectations about the ways in which liquid ‘should’ behave, and also are of critical practical importance to space systems design where examples of such large capillary length scale multiphase flows are commonplace.

1.2 Droplet Electro-Bounce

During the ‘rolling-up’ of droplets under ideal conditions, the spontaneous jump phenomenon is governed by a balance of inertia and surface tension forces, and once aloft the droplet motion is nominally in a regime of pure drag, however other forces can again come into play.

We have observed jumped droplets to occasionally decelerate and return

to the superhydrophobic surface, rebounding multiple times after fashion of rigid body bouncing ounder 1-g. The forces at work in this phenomenon are presumably electrostatic in origin. Though this was an unintended effect in our work on spontaneous droplet jump, but the phenomenon is interesting itself. There is a certain irony to this typical failure of low-gravity intuition (the effect of relatively tiny electrostatic forces becoming suddenly large in the absence of gravity), being as we are experienced low-gravity researchers who perhaps should know better. A time-lapsed composite image showing an example of the phenomenon is shown in Figure 1.1.

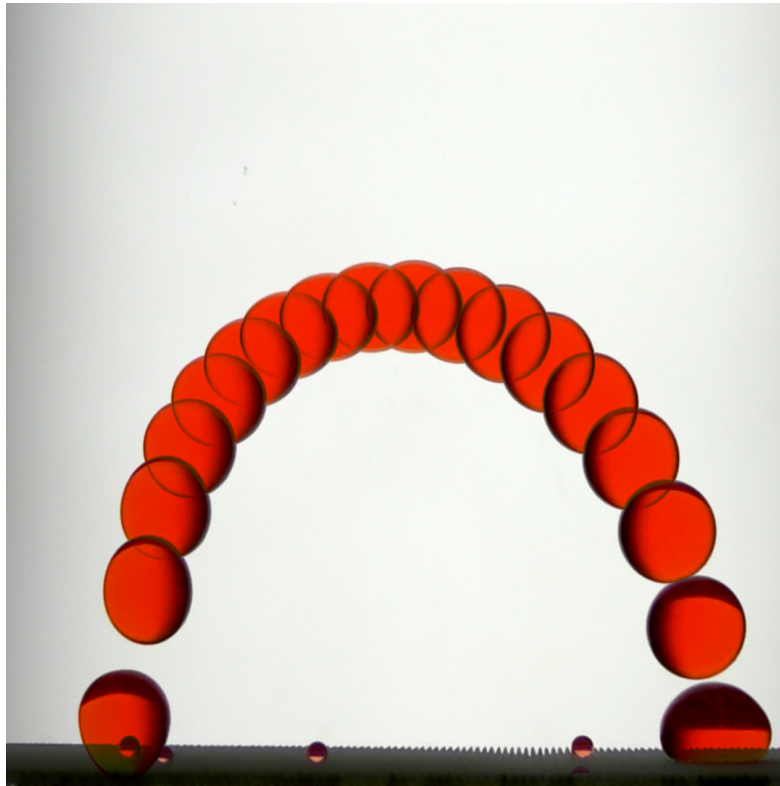


Figure 1.1: The trajectory of a 0.5 mL droplet is captured in a composite image over a single bounce period (~ 1.25 s). The surface potential of the superhydrophobic dielectric in this example is $\varphi_s = 1.25 \pm 0.41$ kV.

This “electro-bounce” phenomenon is the subject of this thesis. We begin with some preliminary observations of the phenomenon:

- Observed droplet (de-)accelerations are on the order of 10’s of cm/s^2 for a range of droplet volumes $V_d \approx 0.03\text{-}0.5 \text{ mL}$.
- The droplets are attracted to regions of high electric field. The horizontal (surface plane parallel) components of the droplet trajectory usually oscillate about their initial position during the experiment (except in cases of nearly pure 1-D vertical translation). For especially small drops close to the spontaneous droplet jump limit ($V_d \sim 0.01 \text{ mL}$) the droplets do not jump, but translate across the surface in a hovering regime until either they reach a local maximum of the electric field, or until their motion is sufficiently damped by contact line hysteresis that pinning arrests their motion.
- The droplets appear to have net free charge. In cases of multiple simultaneous droplet jumps the droplets repel each other as they bounce or hover in orbital motion around regions of high field.
- The magnitude of the droplet trajectory maxima (apoapses) appear to be related to the droplet volume (which affects their mass, and initial jump velocity, and thence their inertia), and to the electric field strength.

There are several possible origins of the electric charge which are ultimately responsible for this phenomenon. It is well known that water acquires free charge (usually positive) when in contact with certain polymers, espe-

cially polytetrafluoroethylene (PTFE) [21], through a process called contact charging. PTFE, on the other hand, tends to readily acquire negative charge by contact with water. The superhydrophobic surfaces used in the spontaneous droplet jump experiments have thin (nanometric) PTFE coatings, and we observe that it is extremely easy to produce significant surface potentials ($\varphi_s \sim 100\text{-}500$ V) by simply flowing streams of distilled water over them. A study of this water on PTFE contact charging phenomenon was done by Yatsuzuka *et al.* [22], who suggest that this process results from formation of an electrical double layer driven by selective adsorption of (OH^-) ions at the polymer surface; other recent work strongly supports this hypothesis [23] [24]. Yatsuzuka *et al.* also found that the specific charge on the droplets in contact with the surface depends on their both surface velocity and conductivity. This contact charge is the most likely accidental source of charge on the superhydrophobic surface. Given the large roughness, or the ratio of projected to actual surface area, of the superhydrophobic surfaces used in the experiment, and given that the droplets are initially in a Cassie-Baxter state, an electrically insulating air layer is maintained that prevents grounding of the droplets despite the large potential difference between them and the surface charges. If this electrostatic potential is greater than the release of surface energy under the sudden change in \mathbb{B}_0 (in the form of the droplet kinetic energy), we expect that the droplet will return to an equilibrium state on the charged surface (minimizing the potential).

The source of the net free charge on the droplets is another issue. The droplet charge could of course also be due to the contact charging mechanism mentioned previously. For instance, in a 1996 paper, NASA flight engineer

Don Pettit discusses the problem of low-gravity flow induced charging of liquids, resulting ultimately from contact charging phenomenon [25]. Another mechanism for the droplet charge is field induced charging. Field induced charging occurs due to physical breakup of a conductor having a field induced dipole (e.g a physical seperation of charge). In our case this occurs when the droplet is deposited on the charged surface by a syringe. The metal syringe needle tip, and the liquid in the syringe itself are essentially a ground connection which is broken when the syringe is removed. Field induced charging is at work in the famous Kevin thunderstorm, and is applied in inkjet, and electrospray technologies (where in each case the breakup is by the Rayleigh-Plateau instability). Notably, in Pettit's discussion of contact charging of liquids in low-g, he remarks on accidental electrostatic "hula-ing" of silicon oil droplets when ejected from a syringe in the vicinity of a highly-charged polymer surface during an experiment conducted aboard STS-5 by mission specialist Joseph Allen. Depending on the (highly-variable) electrical conductivity of the silicon oil, and the material of the syringe used in the experiment, the charge could as easily be field induced as due to contact charging. Relatedly, in a series of informal, and somewhat whimsical experiments Pettit himself electrostatically orbited small water droplets around a triboelectrically charged PTFE knitting needle while aboard ISS during expedition 30/31 [26]. Again, in this case, the droplet charge is very likely field induced.

1.3 Applications

This study of the droplet electro-bounce phenomenon may have results which can be extended to useful applications in a space environment.

External surfaces of spacecraft tend to become charged with time due to the space environment itself. Surface charging largely occurs due to low energy electrons (3-50 keV) which do not penetrate the surface of the spacecraft external structure [27]. The ultimate sources of these charges are trapped charged particles of the van Allen radiation belts, galactic cosmic rays, and the solar wind. This deposited charge accumulates and can lead to significant potential differences between different parts of a spacecraft, sometime leading to breakdown and discharge, called Paschen discharge. Deep dielectric charging occurs when higher energy charged particles penetrate the surface of a dielectric material, which can also lead to large potential differences if the dielectric leakage is lower than the external charging rate. In a fluid mechanical context, this accumulated charge could be problematic during any multiphase venting process, as might be expected to occur during autonomous satellite servicing refueling operations, or during boil-off venting of cryogens stored over long periods in a space environment (as in many crewed Mars mission scenarios, or in cryogenic propellant depot operations). Such venting, if occurring in a region of strong field, will also tend to produce a stream of charged droplets, which can then return and lead to contamination of the spacecraft surfaces.

As previously noted, robust phase separation is critical to high reliability multiphase systems used in thermal control and life support. Active (but

solid-state) phase separation for ECLSS multiphase flows, especially high void-fraction flows is a possible application of this work. Such flows pertain to dish washing, laundry, waste solids drying, food processing, the Sabatier CO₂ reaction, and possibly in vapor-compression cycle condensers. Phase separation for other disperse droplet flows include electrostatic droplet separators for high-efficiency Rankine-cycle turbines (which require a droplet-free vapor phase entering the turbine, but where conventional superheat approaches come with severe mass penalties) [28], or more speculatively, in high temperature liquid droplet radiators with electrostatic collection [29]. Removal of satellite droplets produced during pipetting in wet-lab research outside of a glovebox environment aboard ISS has also been recently suggested as an application of the work [ref, personal discussion with NASA MSFC folk at ASGSR17 conference]. Droplets can become spontaneously charged by contact with standard micropipette tips [30], and this free charge can possibly be leveraged for the purposes of phase separation in low-gravity.

1.4 Overview of this Thesis

In this thesis we develop, and partly validate a simple model to aid in design of future electrostatic disperse droplet phase separators. To that end this work encompasses:

1. A mathematical model of the droplet electro-bounce, its scale analysis, asymptotic estimates for droplet apoapses and times-of-flight.
2. The results of a controlled experiment, where the effect of key indepen-

dent variables droplet volume V_d , and dielectric surface charge density σ , on droplet trajectories is tested.

3. Science of opportunity comprising experimental data on droplet impacts at very low Weber and Ohnesorge numbers, for varying levels of electrostatic Bond number.

Chapter 2

Theory

2.1 Forces and the Equation of Motion

This section will develop a simple, 1-dimensional model of the dynamics of droplets dominated by electrostatic forces. We treat a droplet as a particle, with radius R_d , which translates vertically along the central axis of a finite square charged dielectric sheet with initial velocity U_0 . The equation of motion for this system is given by,

$$my'' = -\mathbf{F}_D - \mathbf{F}_E, \quad y(0) = R_d, \quad y'(0) = U_0, \quad (2.1)$$

where m is the droplet mass, $y'' = \frac{d^2y}{dt^2}$ is the droplet acceleration, \mathbf{F}_D is the drag force, and \mathbf{F}_E is the electrostatic force. The initial conditions are such that, when the \mathbb{B}_0 is suddenly reduced at the start of the drop tower experiment, the droplet jumps with initial velocity U_0 from its 1-g resting position R_d at $t = 0$. The signs of the forces on the right side of Equation

2.1 indicate that they act in opposition direction of the droplet motion. To start to describe the droplet electro-bounce we must define models for each of the forces in this equation.

At intermediate range of Reynolds numbers $\mathbb{R}\text{e} \equiv \frac{2UR_d}{\nu}$, $1 \leq \mathbb{R}\text{e} \leq 5000$ the force of drag acting on the droplet will be quadratic such that,

$$\mathbf{F}_D = \frac{1}{2} C_D \rho A y'^2,$$

where C_D is the drag coefficient, ρ is the density of the surrounding fluid medium (air, in this case), and A is the frontal area of the droplet. For this range of Reynolds numbers it is appropriate to approximate the drag coefficient by the well known Abraham correlation [31],

$$C_D = \frac{24}{9.06^2} \left(1 + \frac{9.06}{\sqrt{\mathbb{R}\text{e}}}\right)^2.$$

Modeling the electrostatic force is somewhat more involved, but we will start with the standard electrohydrodynamic (EHD) approximation [32] as our model, and further simplify where possible. Under a DC electric field, we assume that the real part of the dielectric permitivity ϵ , $\text{Re}\langle\epsilon\rangle \approx \text{constant}$. We also assume that electric currents are small enough that the effects of magnetic fields can be neglected. The validity of this assumption rests on the size of the characteristic time scale for electrical phenomena $\tau_e = \epsilon\epsilon_0/\sigma_e \ll 1$, where τ_e is the ratio of absolute dielectric permittivity $\kappa = \epsilon\epsilon_0$, to conductivity σ_e , of the medium. This characteristic time τ_e is also known as the relaxation time, and is a measure of how quickly the polarization of a dielec-

tric responds to a change in electric field. Given the respective conductivity, and permittivity in the limiting case of extremely-pure water ($\kappa \sim 80$, $\sigma_e = 18.2 \times 10^6 \Omega\text{cm}$) [22], we estimate $\tau_e \approx 4 \times 10^{-6} \text{ s}$. The relaxation time for the common distilled water that is actually used in the droplet experiments is undoubtedly even shorted (due to the presence of solvated ions). Neglecting the effects of a electric double layer on hydration of ions (in the water or the ambient atmosphere) due to the relatively massive size of the droplets studied, then the assumption of small relaxation time further implies that the free charge present in the droplets will remain approximately constant during the typical time interval of a low-gravity experiment.

Supposing that electrical forces acting on free charges and dipoles in a fluid are transferred directly to the fluid itself, then this overall electrical body force will be the the divergence of the Maxwell stress tensor τ_m ,

$$\mathbf{F}_E = \nabla \cdot \tau_m = \nabla \cdot \left(\epsilon \epsilon_0 \mathbf{E} \mathbf{E} - \frac{1}{2} \epsilon \epsilon_0 \mathbf{E} \cdot \mathbf{E} \delta \right),$$

where \mathbf{F}_E is the electric body force per unit volume, and δ is the delta function. The product of the electric field vectors is the dyadic product.

The classical Korteweg-Helmholtz volumetric force density formulation of the Maxwell stress tensor is usually expressed as [33]

$$\mathbf{F}_E = \rho_f \mathbf{E} + \frac{1}{2} |E|^2 \nabla \epsilon - \nabla \left(\frac{1}{2} \rho \left(\frac{\partial \epsilon}{\partial \rho} \right)_T |E|^2 \right). \quad (2.2)$$

The first term in this expression, is the well known Coulombic force or electrophoretic force, which arises from the presence of free charge in an external

electric field. We expect this term to dominate the electric force in a DC field. The second term is the force arising from polarization stresses due to a nonuniform field acting across a gradient in permittivity. This force is widely termed the dielectrophoretic force (DEP). The third term describes forces due to electrostriction. It has been noted by Melcher and Hurwitz that the electrostriction term is the gradient of a scalar and can thus be canonically lumped together with the hydrostatic pressure for incompressible fluids [10]; we neglect it in our analysis.

It is common to approximate the polarization stress by idealizing the droplet as a simple dipole using the effective dipole moment method first described by Pohl in 1958 [34]. This approach has since been related back to the force density by the volumetric integration of the force density with the substitution of a Taylor series expansion of \mathbf{E} in the limit of a small radial gradient of the field within the dielectric sphere [35]. The DEP force is related to the dipole moment (induced or permanent) of polarizable media which has a tendency to align the dipole with the electric field. If there is a gradient in the field then for a finite separation of charge one end of the dipole will feel a stronger electric field than the other, resulting in a net force. Whether the force is positive or negative in the direction of the electric field gradient depends on the difference of dielectric permittivities between the fluids, rather than on the polarity of \mathbf{E} . In principle an external electric field will tend to induce a dipole in a dielectric material, but if the field is spatially uniform there is no gradient in the field and the forces felt by the dipoles are symmetric and thus there is no net force. The dipole moment of a spherical

linear-dielectric particle immersed in a dielectric medium is given by

$$\mu = V_d \mathbf{P} = \frac{4}{3}\pi R_d^3 \mathbf{P}, \quad (2.3)$$

where $\mathbf{P} = (\kappa_1 - 1)\epsilon_0 \mathbf{E} = \chi_e \epsilon_0 \mathbf{E}$ is the polarization moment, and R_d is the particle radius, $\kappa_1 = \frac{\epsilon}{\epsilon_0}$ being the relative dielectric constant of the external medium (air in this case), $\chi_e = \kappa_1 - 1$ being the electric susceptibility of the dielectric medium. The excess polarization \mathbf{P}_e , in the sphere is given by

$$\mathbf{P}_e = (\kappa_2 - \kappa_1)\epsilon_0 \mathbf{E} = \frac{3\kappa_1}{\kappa_2 + 2\kappa_1} \mathbf{E}, \quad (2.4)$$

where κ_2 is the relative dielectric constant of the spherical particle. Taking together Equations 2.3, and 2.4 the effective dipole moment of the particle is given by

$$\mu = 4\pi R_d^3 \left(\frac{\kappa_2 - \kappa_1}{\kappa_2 + 2\kappa_1} \right) \kappa_1 \epsilon_0 \mathbf{E}, \quad (2.5)$$

and the force felt by the dipole is

$$\begin{aligned} \mathbf{F}_{DEP} &= (\mathbf{P}_e \cdot \nabla) \mathbf{E} \\ &= 2\pi R_d^3 \kappa_1 \epsilon_0 K \nabla E^2, \end{aligned} \quad (2.6)$$

where it is nice to use the simplifying shorthand $K = \frac{\kappa_2 - \kappa_1}{\kappa_2 + 2\kappa_1}$, which is also known as the Clausius-Mossotti factor. In cases where $K < 0$, or $K > 0$ the particle will be repelled or attracted to regions of strong field respectively. In our experiment, taking the relative dielectric constants to be $\kappa_1 \approx 1$ and $\kappa_2 \approx 80$, the Clausius-Mossotti factor $K \approx 0.96$. It is important to note

that the equivalent dipole approximation critically requires an assumption of small physical scale of the particle relative to the lengthscale of nonuniformity of the field, which in this case we take to be the length of the charged superhydrophobic surface ($L = 25$ mm $\gg a \approx 2.5$ mm).

When the droplet is close to the dielectric surface, the free charge on the droplet will tend to induce polarization of the dielectric, perturbing the electric field. The polarization bound charge in the dielectric will be of the opposite sign of the free droplet charge and thus there will be a force of attraction. This so-called image force is a correction to the Coloumb force due to the external electric field only, and can be found by the method of images [36]. The image force \mathbf{F}_I , is given by

$$\mathbf{F}_I = \frac{kq^2}{16\pi\epsilon_0} y^{-2} \hat{\mathbf{j}}, \quad (2.7)$$

where the factor k is a function of the dielectric surface susceptibility $k = \frac{\chi_e}{\chi_e + 2}$, and $\hat{\mathbf{j}}$ is a unit vector normal to the dielectric surface.

By substituting Equations 2.6, 2.7 into Equation 2.2 we have

$$\begin{aligned} \mathbf{F}_E &= q\mathbf{E} + \mathbf{F}_{DEP} + \mathbf{F}_I \\ &= q\mathbf{E} + \frac{kq^2}{16\pi\epsilon_0} y^{-2} \hat{\mathbf{j}} + 2\pi R_d^3 \kappa_1 \epsilon_0 K \nabla E^2, \end{aligned}$$

and the 1-D governing equation becomes

$$\begin{aligned} my'' &= -\frac{1}{2} C_D \rho A y'^2 - qE - \frac{kq^2}{16\pi\epsilon_0} y^{-2} - 2\pi R_d^3 \kappa_1 \epsilon_0 K \nabla E^2, \\ y(0) &= R, \quad y'(0) = U_0. \end{aligned} \quad (2.8)$$

By comparing DEP and Coulombic terms in Equation 2.8, we note that a condition to neglect the DEP term is

$$\frac{q}{\kappa_2 \epsilon_0 K R_d^2 E_0} \gg 1$$

As this condition likely holds in our experiments we henceforth neglect the DEP force in our analysis. There is some physical intuition to support this conclusion as well. The dielectric displacement, $\mathbf{D} = \kappa \epsilon_0 \mathbf{E}$ of a water droplet in air is very high due to its large relative dielectric constant. This implies that the field strength within the droplet is about 2 orders of magnitude smaller than in the surrounding medium (which is essentially the same as a vacuum from a dielectric standpoint), thus it is not particularly inaccurate to model the dielectric volume of a droplet as a conductive shell (an equipotential), with zero field in its interior. As an aside, in treating the droplet as an ideal conductor we note that in our specific case the electrostatic force is not a body force *per se* as the electric field is acting on charges on the surface of the conductor.

2.2 The Electric Field

If we consider the charged dielectric surface of our experiments to be a square sheet of charge lying in the xz -plane with width L , the symmetry of the problem happily lets us obtain the y -component of the electric field \mathbf{E} by direct integration. In particular it is easy to construct the electric field due to a finite plane of charge by superposition of the electric fields of a series

of line charges. By symmetry the electric field points along the y -axis; for a point along the y -axis the position vector is $\mathbf{r} = (x^2 + y^2)^{1/2} \hat{\mathbf{r}}$ to the center of a line charge in the xz -plane. The y -component of $d\mathbf{E}$ is found by $dE_r = dE_y \cos \theta = dE_y y/r$, where θ is the angle made between the y -axis and the position vector \mathbf{r} . If the charge in a line element, dx is $\sigma L dx$, where σ is the average surface charge density, the electric field of a line charge is given by [36]

$$dE_r = \frac{k\sigma L dx}{4\pi\epsilon_0 r \sqrt{r^2 + L^2/4}}.$$

The y -component of the electric field E_y , is then

$$E_y = \frac{\sigma Ly}{4\pi\epsilon_0} \int_{-L/2}^{L/2} \frac{1}{(y^2 + x^2) \sqrt{y^2 + x^2 + L^2/4}} dx.$$

With some substitutions this can be integrated to obtain an expression for the electric field in terms of y ,

$$E_y = \frac{\sigma}{\pi\epsilon_0} \tan^{-1} \left(\frac{L^2}{y\sqrt{2L^2 + 4y^2}} \right). \quad (2.9)$$

We note that this model of the electric field will be poor except in cases where $y \ll L$, $R_d \ll L$, which will be true for cases of large drops very close to the dielectric surface. For accurate models of the field in this case we likely would need to solve Laplace's equation for the electric potential φ

$$-\nabla^2 \varphi = 0,$$

numerically using finite element methods.

By taking Taylor series expansions in large and small limits we can intuit a bit about the behavior of this field. In the limit $L \rightarrow \infty$, $y \ll L$ the argument of the function tends towards infinity and

$$\lim_{x \rightarrow \infty} \tan^{-1}(x) = \frac{\pi}{2},$$

and thus

$$E_y \approx \frac{\sigma}{4\pi\epsilon_0} = E_0 \quad y \ll L, \quad (2.10)$$

where E_0 is the characteristic electric field given by $E_0 = \frac{\sigma}{4\pi\epsilon_0}$. This field is constant, and equivalent to the electric field due to an infinite plane of charge. In the limit of $y \gg L$, the argument of the arctangent function can be approximated by

$$\frac{L^2}{2y(2L^2 + 4y^2)^{1/2}} = \frac{L^2}{4y^2(1 + L^2/2y^2)^{1/2}} \approx \frac{L^2}{4y^2}.$$

For small x , $\tan^{-1}(x) \sim x$ and we thus find the familiar electric field due to a point charge

$$E_y \approx L^2 E_0 y^{-2} \quad y \gg L. \quad (2.11)$$

Both of these regimes can be clearly seen in the plot of E_y shown in Figure 2.1.

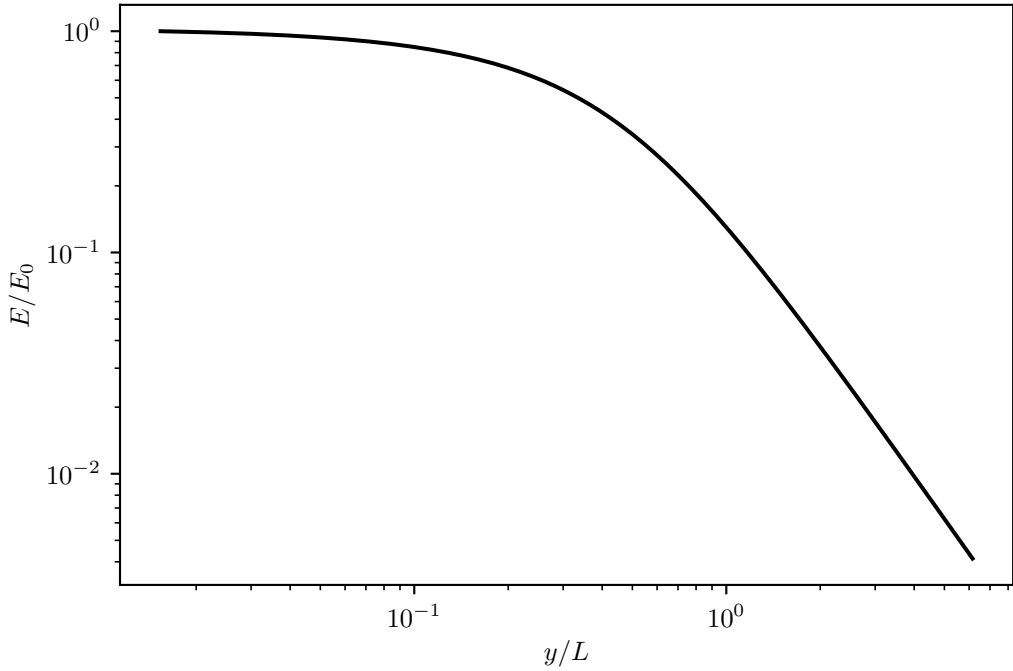


Figure 2.1: A log-log plot of the magnitude of the non-dimensional electric field, E_y .

2.3 Scaling

The equation of motion is non-linear, non-homogeneous and is best solved numerically, but nevertheless we are curious if we can obtain approximate solutions to the equation analytically using perturbation methods. This is aided by non-dimensionalizing the governing equations, and seeing if any dimensionless groups exist, and whether any are particularly small or large, and whether any fortuitous opportunities for simplification appear. Introducing the scaled variables

$$\bar{t} = \frac{t}{t_c}, \quad \bar{y} = \frac{y}{y_c}, \quad (2.12)$$

where y_c and t_c are characteristic length and time scales respectively, and using the coordinate transformation $y(0) - R = 0$, the governing equation becomes

$$\begin{aligned}\bar{y}'' &= -\frac{1}{2} \frac{C_D \rho A y_c}{m} \bar{y}'^2 - \frac{q E_0 t_c^2}{m y_c} \bar{E}(\bar{y}) - \frac{k q^2 t_c^2}{16 \pi \epsilon_0 R^2 m y_c} \left(\frac{y_c}{R} \bar{y} + 1 \right)^{-2}, \\ \bar{y}(0) &= 0, \quad \bar{y}'(0) = \frac{U_0 t_c}{y_c}.\end{aligned}\tag{2.13}$$

We note the existence of several dimensionless groups

$$\Pi_1 = \frac{C_D \rho A y_c}{2m}, \quad \Pi_2 = \frac{q E_0 t_c^2}{m y_c}, \quad \Pi_3 = \frac{k q^2 t_c^2}{16 \pi \epsilon_0 R^2 m y_c}, \quad \Pi_4 = \frac{y_c}{R}, \quad \Pi_5 = \frac{U_0 t_c}{y_c}.$$

2.3.1 Inertial Electro-Image Limit

In the limit of small y and t we expect inertia to scale as Coulombic and image force. In this limit we can approximate the electric field as the constant, E_0 . One possible characteristic length scale is $y_c \sim R_d$, however this ultimately is a poor choice. With $y_c \sim U_0 t_c$ and picking t_c such that Coulombic force is $\mathcal{O}(1)$, the intrinsic scales become

$$t_c \sim \frac{m U_0}{q E_0}, \quad y_c \sim \frac{m U_0^2}{q E_0}.$$

With these scales the governing equation then becomes

$$\begin{aligned}\bar{y}'' &= -1 - \text{Im} (\mathbb{E} u \bar{y} + 1)^{-2}, \\ \bar{y}(0) &= 0, \quad \bar{y}'(0) = 1.\end{aligned}\tag{2.14}$$

with

$$\text{Im} \equiv \frac{kq}{16\pi\epsilon_0 R_d^2 E_0} = \boldsymbol{\Pi}_3, \quad \text{Eu} \equiv \frac{mU_0^2}{qE_0 R_d} = \boldsymbol{\Pi}_4,$$

where Im is the Image number, and denotes the ratio of image forces to the Coulombic force of the unperturbed field, and where Eu is the electrostatic Euler number, and is a ratio of inertia to electrostatic force. With these dimensionless groups the intrinsic scales become

$$t_c = \text{Eu} \frac{R_d}{U_0}, \quad y_c = \text{Eu} R_d.$$

2.3.2 Inertial Electro-Viscous Limit

In the limit of large y and t we expect droplet inertia to scale as Coulombic force and drag. In this limit we approximate the electric field as $E \approx y_c^2 E_0 y^{-2}$. In this case there are several (obvious) possible choices of scales:

1. $y_c \sim U_0 t_c$, and make Coulomb force $\mathcal{O}(1)$.
2. $y_c \sim L$, $t_c \sim \frac{L}{U_0}$ (however, this makes Equation 2.13 singular).
3. $y_c \sim L$, $t_c \sim \left(\frac{L m}{q E_0}\right)^{1/2}$.
4. $y_c \sim L$, and make Coulomb force $\mathcal{O}(1)$.

We prefer the approach with the greatest physical simplicity, fewest Pi terms, and that has homogeneous initial conditions. We choose Case 1, where the intrinsic scales are given by

$$t_c \sim \frac{R_d^2}{L^2} \frac{4\pi m U_0}{q E_0}, \quad y_c \sim \frac{R_d^2}{L^2} \frac{4\pi m U_0^2}{q E_0}.$$

With this scaling the non-dimensional governing equation is

$$\begin{aligned}\bar{y}'' &= -\mathbb{D}g\mathbb{E}u_+\bar{y}'^2 - (\mathbb{E}u_+\bar{y} + 1)^{-2}, \\ \bar{y}(0) &= 0, \quad \bar{y}'(0) = 1\end{aligned}\tag{2.15}$$

where we call $\mathbb{D}g$ the drag number, $\mathbb{D}g \equiv \frac{C_D \rho_a}{\rho_l} = \Pi_1 \mathbb{E}u_+^{-1}$ and $\mathbb{E}u_+ = 4\pi \frac{R_d^2}{L^2} \mathbb{E}u$.

2.4 Asymptotic Estimates

2.4.1 Inertial Electro-Image Limit

The alternate scalings of the equation of motion given by Equations 2.14, and 2.15 are weakly non-linear differential equations in the sense that they reduce to linear equations as the parameter $\mathbb{E}u \rightarrow 0$. If we take $\mathbb{E}u$ to be a small parameter ϵ , we can find an asymptotic approximation to the solution of the non-linear equation by means of a regular perturbation. In this case we use the naive expansion

$$\bar{y}(\bar{t}) \sim \bar{y}_0(\bar{t}) + \epsilon \bar{y}_1(\bar{t}) + \epsilon^2 \bar{y}_2(\bar{t}) \dots \epsilon^n \bar{y}_n(\bar{t}).$$

By substitution of the expansion (and its derivatives) into the differential equation, and equating terms by order, and using the notation $\alpha = \text{Im}$ (this being the equation scaled in the small-times limit), we first find the $\mathcal{O}(1)$,

unperturbed, solution to the equation of motion to be

$$\bar{y}_0(\bar{t}) = \bar{t} + \frac{\bar{t}^2}{2} (-1 - \alpha).$$

Looking at this solution it is evident that if we let $\alpha = 0$, the solution is the classical kinematic equation for projectile motion without drag under constant gravity, g_0 . Continuing on with this procedure we find, (after some tedious computations, documented in in the project repository for this thesis [37]) the higher order composite solutions to be

$$\begin{aligned} \bar{y}(\bar{t}) &= \bar{t} + \frac{\bar{t}^2}{2} (-1 - \alpha) + \epsilon \left(\frac{\alpha \bar{t}^3}{3} + \frac{\alpha \bar{t}^4}{12} (-1 - \alpha) \right) \\ &+ \epsilon^2 \left(-\frac{\alpha \bar{t}^4}{4} + \frac{\alpha \bar{t}^5}{60} (9 + 11\alpha) + \frac{\alpha \bar{t}^6}{360} (-9 - 20\alpha - 11\alpha^2) \right) + \mathcal{O}(\epsilon^3) . \end{aligned}$$

In fact we, for somewhat arbitrary reasons, computed an $\mathcal{O}(\epsilon^5)$ accurate solution, but it is far to ugly to reprint here in its entirety. However, we plot these approximate short-time scaled solutions with varying values of the Image number, $\mathbb{I}m = \alpha$ in Figure 2.2. These plots show a trend of decreasing time-of-flight (the time for the droplet to return to the origin, or complete a single “bounce”), and height at apoapse with increasing values of the Image number α . When $\alpha = 1$ the time of flight is exactly half of characteristic time scale in this regime. In the limit of small ϵ the trajectories collapse to the $\mathcal{O}(1)$ solution regardless of the Image number. In principle there is some coupling between $\mathbb{E}u$ and $\mathbb{I}m$; notably this relationship does not depend on the electric field E_0 but on a charge to mass ratio. The effect of contact line hysteresis on the initial jump velocity U_0 will also tend to independently

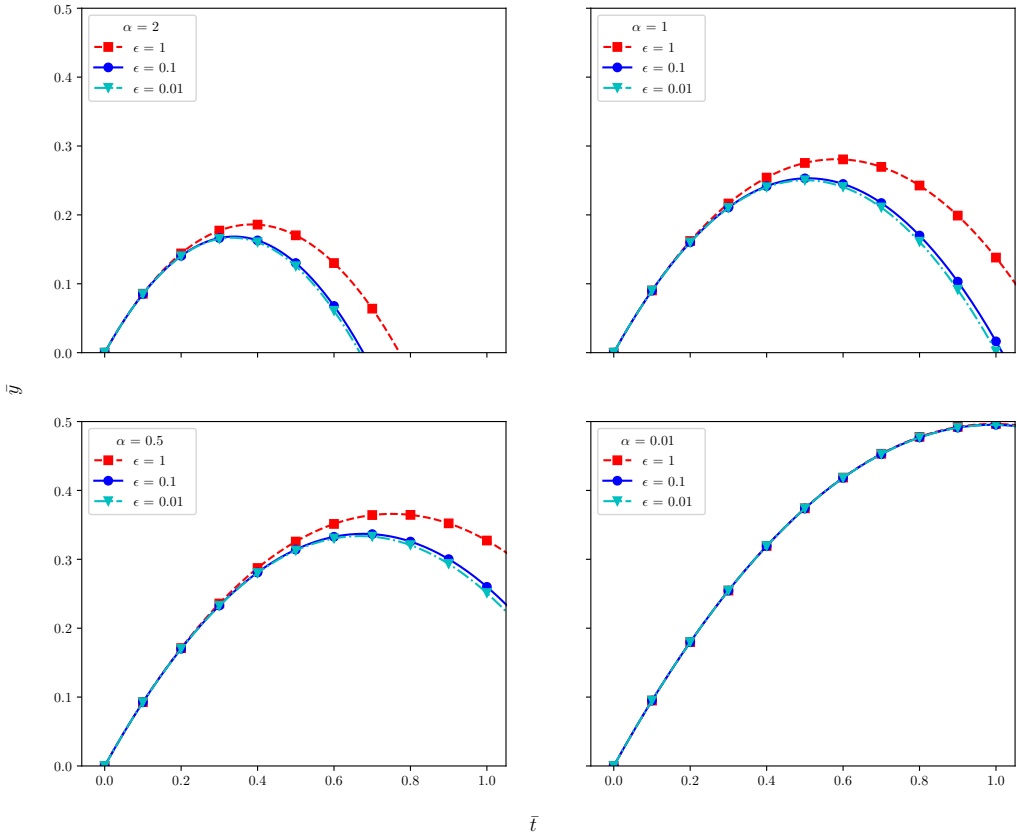


Figure 2.2: Non-dimensional droplet trajectories for various values of $\text{Eu} = \epsilon$, $\text{Im} = \alpha$. The trajectory reduces to the classical $\mathcal{O}(1)$ solution for small values of α . It should be noted that despite what is implied by these plots α is not necessarily completely independent of ϵ , as they share q , and E_0 as common factors, $U_0 \sim R_d^2$, and $m \sim R_d^3$.

decohere the natural covariance between these parameters.

2.4.2 Inertial Electro-Viscous Limit

By similar arguments we find an asymptotic estimate of the trajectory in the long-times scaled regime. With $\epsilon = \text{Eu}_+$, where ϵ again is a small parameter,

and $\beta = \mathbb{D}g$, the approximate solution is

$$\begin{aligned}\bar{y}(\bar{t}) &= \bar{t} - \frac{\bar{t}^2}{2} + \epsilon \left(\frac{\bar{t}^3}{3} (1 + \beta) + \frac{\bar{t}^4}{12} (-1 - \beta) - \frac{\beta \bar{t}^2}{2} \right) \\ &+ \epsilon^2 \left(\frac{\bar{t}^4}{12} (-3 - 3\beta - 4\beta^2) + \frac{\bar{t}^5}{60} (11 + 10\beta + 8\beta^2) + \frac{\bar{t}^6}{360} (-11 - 10\beta - 8\beta^2) + \frac{\beta^2 \bar{t}^3}{3} \right) \\ &+ \mathcal{O}(\epsilon^3)\end{aligned}.$$

This trajectory given by this solution is shown in Figure 2.3. If we assume a constant scale for the drag coefficient, $C_d \approx 0.5$, then the Drag number $\beta = \mathbb{D}g$ is approximately a constant $\beta \approx 6 \times 10^{-4}$ in all of our experiments. Again, the trajectory seemingly reduces to the classical $\mathcal{O}(1)$ solution for

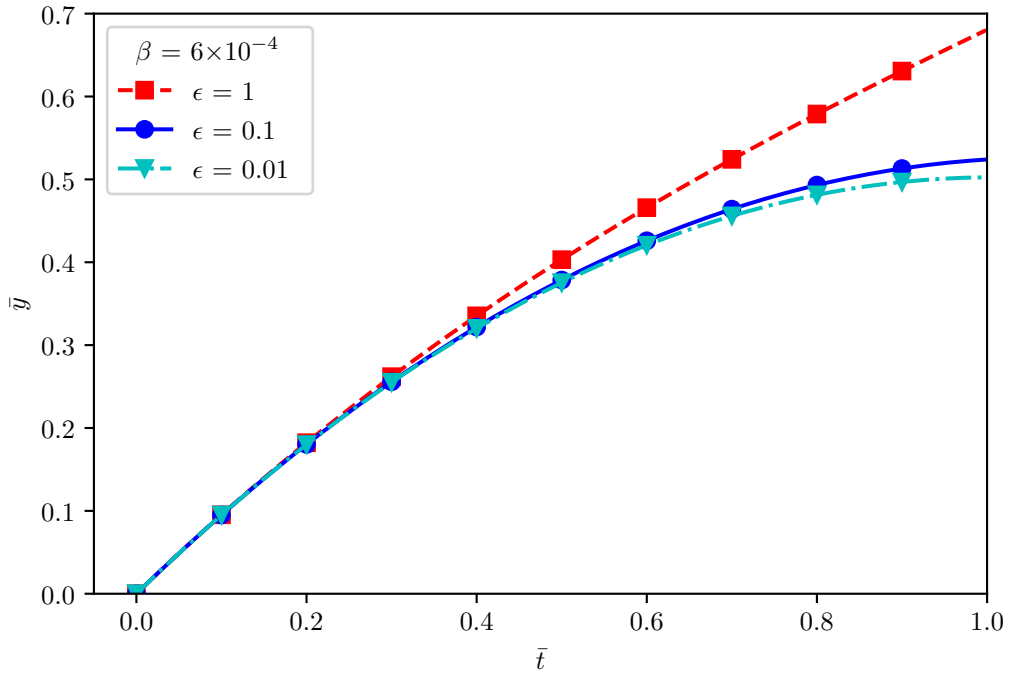


Figure 2.3: Non-dimensional droplet trajectories for various values of $\mathbb{E}u = \epsilon$.

small values of ϵ . We also note that the effect of drag is very slight, appearing only as a slight correction to the higher order terms; the apoapse

is very nearly equal to half the characteristic length scale. In practical terms this linearizing effect of small β may disappear if the fluid density is much less than that of water, as in our experiments.

By again applying a regular perturbation to the asymptotic solution with the expansion

$$\bar{t} \sim \bar{t}_0 + \epsilon \bar{t}_1 + \epsilon^2 \bar{t}_2 \dots \epsilon^n \bar{t}_n,$$

and solving for the roots (that is, the times when $\bar{y} = 0$), we find an asymptotic estimate for the time-of-flight, t_f . The $\mathcal{O}(\epsilon^2)$ accurate time-of-flight estimate is given by

$$t_f = 2 + \epsilon \left(\frac{4}{3} - \frac{2\beta}{3} \right) + \epsilon^2 \left(\frac{4}{5} - \frac{4\beta}{3} + \frac{2\beta^2}{5} \right) + \mathcal{O}(\epsilon^3).$$

Substituting the experimental value of β we find the time-of-flight estimate for water droplets in air to be

$$t_f = 2 + 1.333\epsilon + 0.799\epsilon^2 + \mathcal{O}(\epsilon^3) \quad (2.16)$$

In Figure 2.4 we look at the effect of increasing values of $\mathbb{E}u_+$ on time-of-flight. We see that as ϵ grows to be no longer small, the time-of-flight grows rapidly, but this behavior appears to have an asymptote at a certain critical velocity as $\mathcal{O}(\mathbb{E}u_+) \rightarrow \mathcal{O}(1)$; this is an electrostatic escape velocity, U_e . We can find the escape velocity by solving a modified version of the equation of motion,

$$mu' = -\frac{qE_0}{y^2},$$

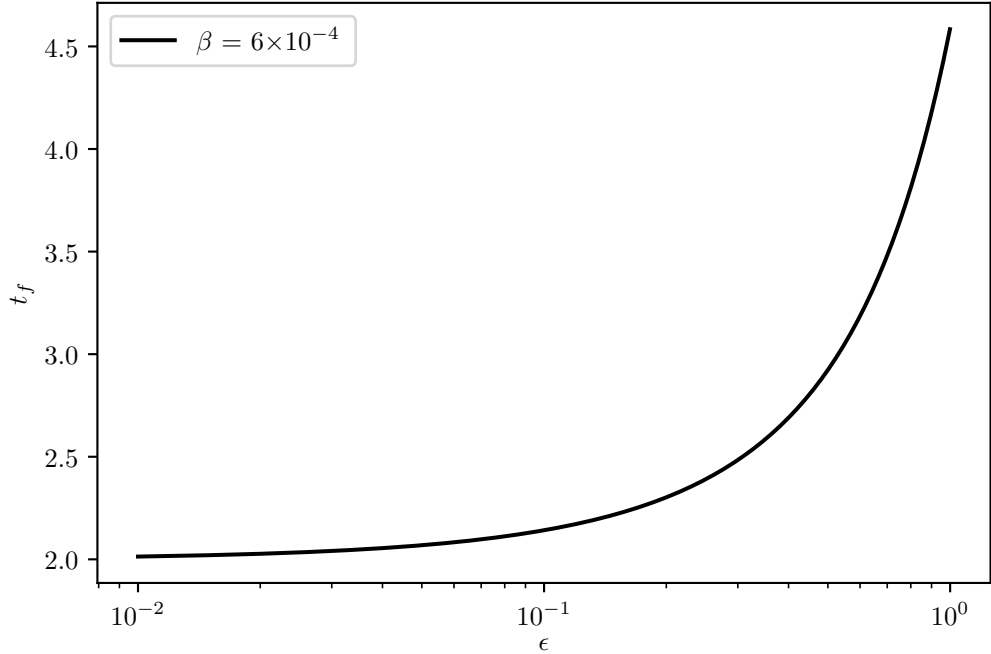


Figure 2.4: $\mathcal{O}(\epsilon^3)$ asymptotic estimate of droplet time-of-flight as a function of $\epsilon = \mathbb{E}u_+$.

where $u = \frac{dy}{dt}$ is the droplet velocity. Integrating between the respective limits,

$$m \int_{U_0}^{u(y)} u du = -qE_0 \int_{R_d}^y \frac{dy}{y^2},$$

which has the solution

$$u(y) = \pm U_0 \left[1 + \frac{2qE_0}{mU_0^2} \left(\frac{1}{y} - \frac{1}{R_d} \right) \right]^{1/2}.$$

This equation has an asymptotic velocity, U_∞ at $y = \infty$ which is real if

$$U_0 \geq U_e = \sqrt{\frac{2qE_0}{mR_d}},$$

where U_e is the escape velocity and $U_\infty = \sqrt{U_0^2 - U_e^2}$. The condition for the droplets to escape the electric field is then given by

$$\mathbb{E}u_+ > 1/8\pi. \quad (2.17)$$

Referring again to Figure 2.4, we suspect that there is perhaps a better choice of scaling available, as the time-of-flight estimate is not asymptotic at $\mathbb{E}u_+ = 1/8\pi$.

If the droplet escapes the electric field it will have a residual velocity U_∞ , and will be in a regime of pure inertia \sim drag. The velocity will then decay as

$$\bar{u}(\bar{t}) = \frac{1}{\bar{t} + 1},$$

with a characteristic time $t_c \sim \frac{2m}{C_D \rho A U_\infty}$, which is the halving time of the velocity.

Chapter 3

Methodology

3.1 Overview

Mainly we are concerned about what parameters are important in electrostatic transport of relatively large (e.g. millimetric) droplets in low-gravity, and what the values of the respective dimensionless groups, namely \mathbb{I}_m , \mathbb{E}_u and \mathbb{E}_{u+} might be. To find typical vales of these parameters we used the following approach:

1. We observed spontaneous droplet jumps on charged dielectric superhydrophobic surfaces under low-gravity conditions in a 2.1 s drop tower, while varying the independent variables V_d , σ . However, this raises an interesting challenge; it is impractical to directly measure all of the key physical quantities that appear in the dimensionless groups at once in a drop tower experiment. In particular, determination of net droplet free electric charge q , is difficult (as high-input resistance electrometers, being notoriously fickle instruments, are not well suited to sudden 15-g

decelerations). Schematic representations of the droplet jump, and of the droplet in the Cassie-Baxter 1-g initial state is shown in Figures 3.2 and 3.1.

2. Using high-speed video and image analysis software we captured the trajectories of the droplets.
3. We solved the inverse problem to find the key parameters by maximizing a statistical likelihood function between an observed trajectory and the trajectory predicted by a dynamical model given that certain set parameters. The best fit parameters obtained by direct-search optimization are those corresponding to the maximum likelihood experimental values. The optimization is constrained by the measurement precision of directly measured independent, and dependent variables.

3.2 Experimental Methods

The DDT uses a dual capsule design, inspired by the 2.2 s facility at NASA Glenn Research Center, which decouples drag acceleration felt by the external drag shield from the experiment. The experiment then experiences approximately 1×10^{-6} g of high quality free-fall for the 2.1s required for the rig/drag shield assembly to plummet to the bottom of drop tower 6 floors below. Single droplets of distilled water, in a range of volumes ($0.01 \leq R_d \leq 0.5$ mL), were very carefully deposited on the charged superhydrophobic surface using an grounded glass syringe with $\pm 1 \mu\text{L}$ accuracy, and then dropped in the drop tower. Red dye was added to improve thresholding accuracy in

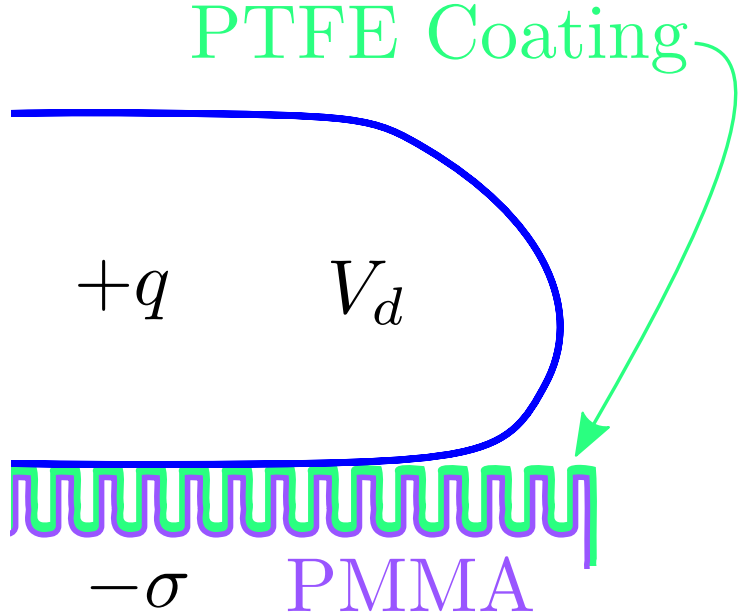


Figure 3.1: A schematic representation of the droplet initial condition, resting on the superhydrophobic surface in the Cassie-Baxter state just prior to the drop tower experiment. The variables q , σ , and V_d are the droplet net free charge, dielectric surface charge density, and droplet volume respectively.

trajectory digitization. Droplet trajectories were recorded using a *Panasonic HC-WX970 Camera*, at 120 fps and 1/3000s shutter speed. In a few cases where higher frame rates were needed a *Nikon 1 J1* camera with a 30mm telephoto lens was used, shooting at 400 fps. The experimental test cell was illuminated with a 6000K LED strip, with a thin semi-opaque plastic film covering to make the light diffuse.

Rather than haphazardly contact charge the surfaces with streams of water, as likely happened by accident in the experiments which inspired this inquiry, we strive for a more controlled, uniform surface charge distribution. Following from this desire, superhydrophobic electrets were prepared, with surface potentials $\varphi_s = 0.7\text{-}4.0$ kV. According to a review by Sessler [38], an

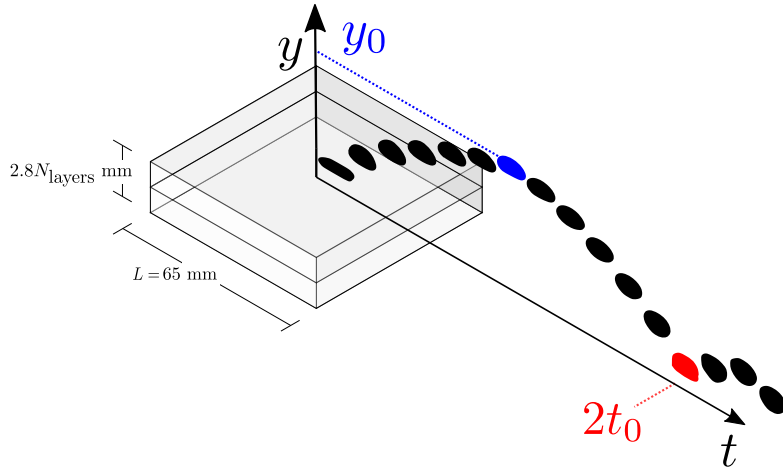


Figure 3.2: A schematic representation of a droplet electro-bounce experiment with labeled characteristic time and length scales, t_c , y_c shown. Also shown are the dimensions of the superhydrophobic electret substrate.

electret is a dielectric material with “quasi-permanent” electric charge in the sense that the characteristic decay period of the electret is much greater than a practical experiment time scale. Electret charge may be ‘true’ charge in the form of surface or space charges, or polarization charges (such as bound charges). If the electret is not screened by a conductor then it produces an external electric field if the polarization and real charges do not uniformly compate each other throughout the volume of the electret. For this reason electrets are thought of as electrostatic analogs to permanent magnets (and the name *electret* itself is a portmantau to that effect conjured by Heaviside in 1892 [39]). Typical commerical electrets are Teflon type (PTFE) polymer films on the order of 10-50 μm thick with the charge being primarily real surface charge. Electrets have a plethora of applications, but most germanely they have been used in Electro-Wetting On Dielectric (EWOD) devices for low-voltage manipulation of small droplets [40]. Real charge elec-

trets can be produced by contact electrification, injection or deposition) of charge carriers by discharge or electron beam, ionizing radiation, or by frictional triboelectrification. Dipolar electrets by contrast are produced by a combination of polarization at elevated temperatures in a strong external electric field, followed by an annealing process. Effective surface charge densities are limited to the material dielectric strengths due to internal dielectric breakdown phenomenon (this typically occurs before external breakdown or Paschen breakdown).

We use an isothermal electret formation process using a variation of the widely applied corona-charging technique. The typical corona-charging technique uses strong inhomogenous DC electric fields to produce discharge in air at ambient conditions; the dielectric substrate is atop a grounded electrode, and there is a screening potential electrode intermediately positioned to control the surface potential (the the surface potential of the dielectric will tend to saturate at this grid potential if the material is not space-charge current limited). The corona field is usually produced by pin-shaped electrode. In air the most common charge carriers thus produced are CO_3^- ions. This approach is known to generally produce samples with fairly uniform surface charge densities. Some work by van Turnhout in 1975 showed, using Thermally Stimulated Current (TCS) measurements, that in 4.8 mm thick polymethyl methacrylate (PMMA) polarization of the dielectric is non-uniform, due to real space-charge mostly ($\sim 90\%$) residing in a thin (0.1-0.2 mm) layer near the free-surface of the sample [41]. In this work we use a balanced AC corona ion source (Ptec IN5120), to direct a net neutral stream of ions towards the dielectric target, which we polarize by an electrode with a 2 kV+

(absolute reference) DC-DC converter. The ion stream compensates the surface and space bound charges arising due to the polarization of the dielectric. When the DC-DC converter is switched to ground, the deposited negative ions remain on the surface.

The electret is lamina of 3-4 0.4 mm thick corona charged PMMA sheets. The electric field strength scales with the number of dielectric lamina as has also been shown in work on electret based vibrational energy harvesters [42] and in water desalinization [43].

The final, superhydrophobic layer, is produced by laser etching PMMA, and depositing a thin layer of PTFE on the resulting roughness topology to increase the Young's angle. The surface charge density can be modulated during the experiment using the high-voltage DC-DC converter, which can re-polarize the dielectric substrate by means of an embedded electrode, and the resulting bound charge partially or fully neutralizes the electric field due to the surface ions deposited by corona charging of the electret. The high-voltage system is armed manually before the drop and is automatically safed by a high-voltage power switching relay, which switches the load across a $100\text{ k}\Omega$ resistor when triggered by the resumption of 1-g conditions. The safing is set by an accelerometer pin-interrupt triggered microcontroller command.

The rig with a mounted experiment is shown in Figure 3.3.

Contact angles of distilled water on the electret $\sim 150^\circ$. The hysteresis of the contact angle (the difference between the advancing and receding contact angles) is estimated from the roll-off angle using the method of Furmidge, 1962 [44], and is found to be approximately 20° when the surface is uncharged. The innate Young's angle hydrophobicity of the PTFE layer is

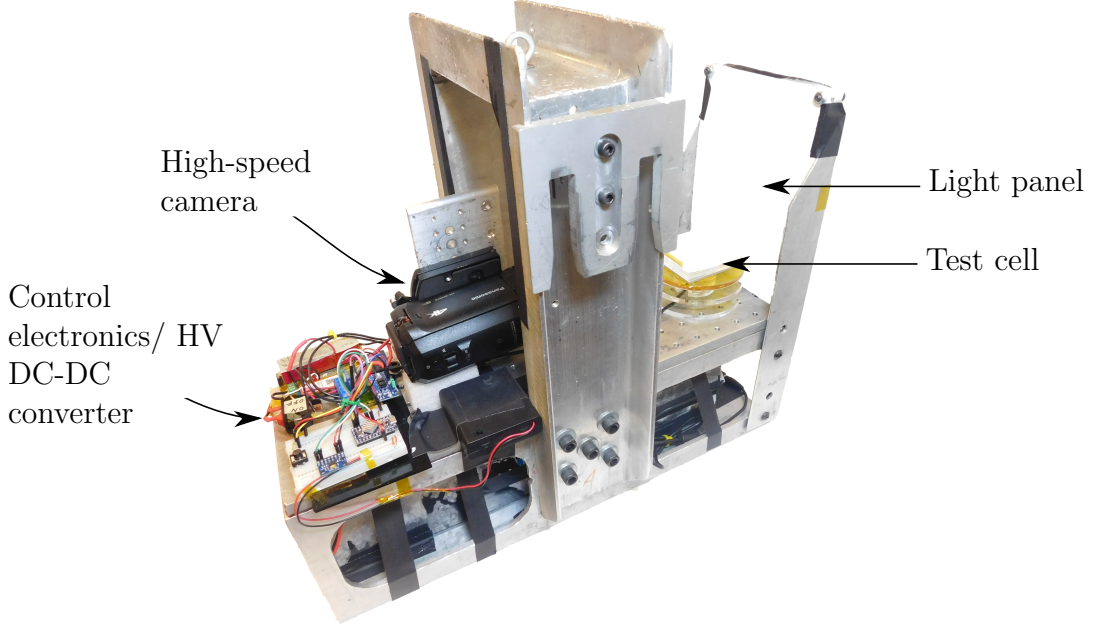


Figure 3.3: The droplet electro-bounce experiment hardware mounted on a drop tower rig.

enhanced by the underlying roughness length scales of the surface. We use a laser-etched pillared geometry with pillar heights $\sim 775 \mu\text{m}$, widths $\sim 70 \mu\text{m}$ and pitch $\sim 100 \mu\text{m}$. An SEM image of the pillar geometry is shown in Figure 3.5.

Surface potentials φ_s , were measured on the superhydrophobic surface using a *Simco-Ion* FMX-004 electrostatic fieldmeter and the method for determination of surface charge density for low conductivity polymers described in Davies, 1967 [45]. This measurement was done with the superhydrophobic surfaces connected by a conductive ground plane by conductive tape, far away from the presence of other conductors. An ideal approach to determining surface charge on a dielectric surface is to screen perturbing effects of external electric fields. This is partly accomplished by grounding the field-

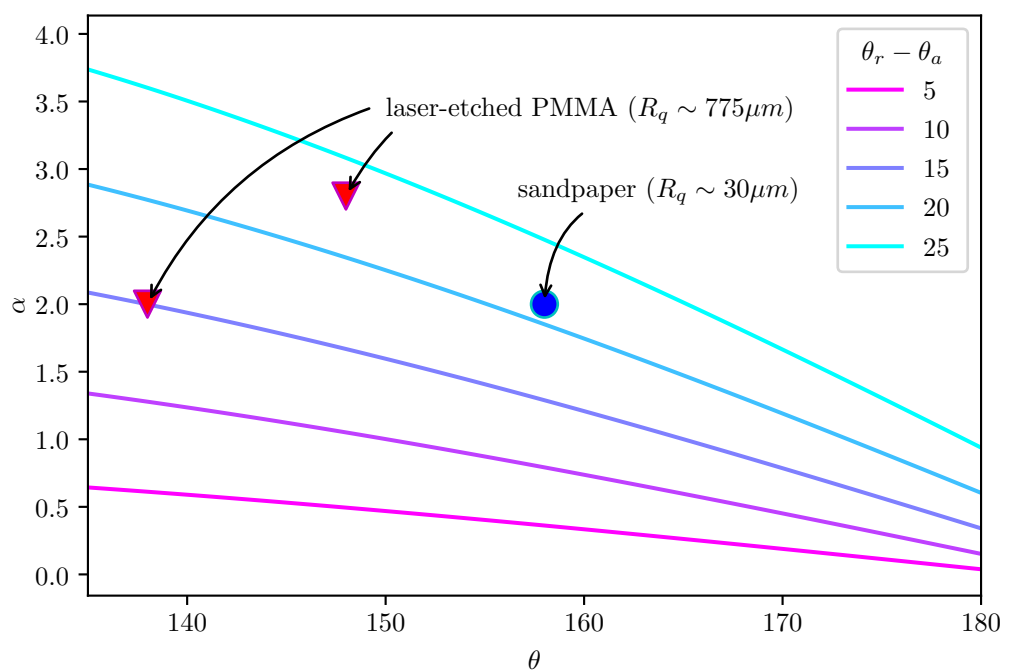


Figure 3.4: Hysteresis of the contact line plotted as a function of static contact angle and roll-off angle for 1 mL droplets.

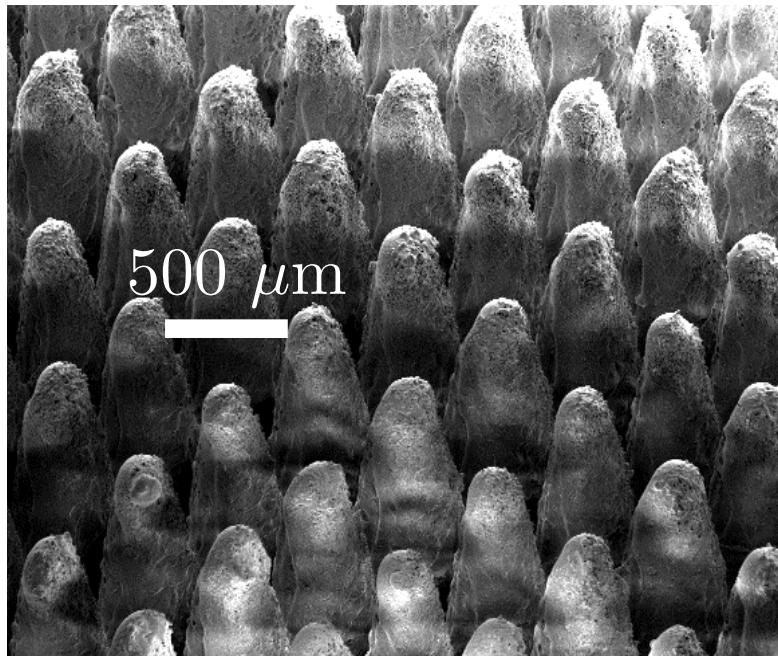


Figure 3.5: SEM image of the superhydrophobic surface.

meter, and by placing the dielectric sample on a grounded conductive plate backing. In this case the surface charge density is determined from

$$\sigma = \frac{\varphi_s \kappa}{l},$$

where l and κ are the thickness of the dielectric surface, and the absolute permittivity respectively. The measured surface voltage is a function of position away from the charged dielectric. In most cases this function is relatively constant at a distance about 1-2 cm away from the surface (there is some measurement error in surface voltage due to small mispositioning of the electrostatic fieldmeter, say by ± 1 mm). The relative dielectric constant of the PMMA sheet was measured by using a 65×65 mm polished aluminum parallel plate capacitor with $C = \epsilon \epsilon_0 \frac{A}{l}$ where C is the capacitance, and A is

the sheet area. Measuring the capacitance with 3 sample thicknesses using a GenRad 1657 RLC Digibrige, we found the relative permittivity to be $\epsilon = 3.5 \pm 0.4$.

A further consideration is the possibility of the change in total charge during a typical experimental timescale. If we consider the drop rig to be a ground (which seems reasonable given that the rig is isolated from true ground, but is at some reference voltage with respect to the surface charges on the dielectric, it also has an abundance of free charge carriers, that is, if it is conductive), then there will be both bulk and surface decay of the charge on the dielectric. The evolution of the charge can in some cases be approximated by

$$\sigma = \sigma_0 e^{\frac{-t}{\epsilon\rho}},$$

where σ_0 is the initial surface charge density, and ρ is the bulk resistivity (which can also be reframed in terms of conductivity by $\rho = 1/\gamma$, where γ is the conductivity). For an example case of a surface with an initial surface charge density $\sigma = 2.4 \times (10^{-6}) \text{ C/m}^2$, relative permittivity $\epsilon = 3.5$ and bulk resistivity $\rho = 1.6 \times (10^{16}) \Omega\text{cm}$ such as with the case of 2.8 mm PMMA sheet, then the time constant $\tau = \kappa\rho$ is approximately 5000 s, which is a great deal longer than the typical time period for of a drop tower experiment. We measured the charge decay with a calibrated probe at periodic intervals. There are several charge decay mechanisms: internal ones, such as Ohmic resistance, and external ones such as compensation by environmental ionic species. The relative magnitudes of these charge transport mechanisms, and therefore the stability of the electret varies drastically depending on its initial surface po-

tential, material properties, environment, and charging method. In the case of unshielded electrets compensation by atmospheric ions is significant [46]. Because environmental convection will tend to maintain a gradient of these ions, sealing an electret in a container from the atmosphere will effectively halt this decay mechanism. Atmospheric humidity and water droplet condensation also significantly increase charge decay (presumably by reducing the surface resistance) [47]. Examples of this decay can be seen in Figure 3.6 for differing numbers of dielectric lamina used in this experiment. In looking at the trends in charge decay for our electrets we notice firstly, that the decay does not appear to be exponential, as in the model described above. Secondly, we plainly see a cross-over effect in the decay of the surface potential in our electret samples, whereby the samples charged to higher initial surface potentials decayed faster and reached the lower overall final potentials. This is a well known effect in polyethylenes charged by corona [48].

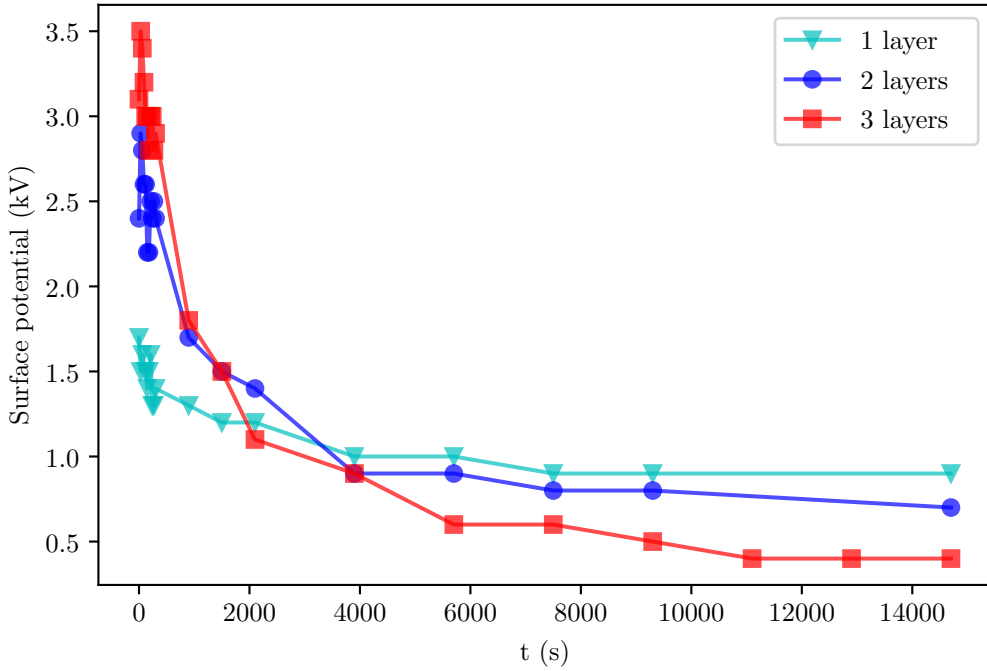


Figure 3.6: Charge decay in the dielectric laminates for differing numbers of layers.

3.3 Data Munging

Digitization of droplet trajectories requires several steps of post-processing. Video is first decomposed into a sequence of still images. Trajectories are captured using the particle tracking module in *Fiji* [49], a derivative of the popular *ImageJ* [50] package for scientific image analysis. The series is stabilized to remove the effect of drop transients from the kinematic data [51]. The series of still images is cropped, and the background (that is, the low-entropy pixels) of the series is removed using a built-in “rolling ball” algorithm. Each still is then split into its constituent RGB maps. In this case the green channel images contained the most information, so these were then globally thresholded using the Triangle algorithm to recover a map of the

pixels corresponding to the droplet’s approximate position in the original still. Ellipses are fitted to the pixel map stepping through the time series to determine the positions of the center of mass, and the semi-major and minor axes of the droplets during the drop. Finally, a perspective correction is applied to the center-of-mass positions.

The code used in this work, as well as the raw data, and the make files for this thesis are archived on the open-source project portal Github [37].

3.4 Parameter Estimation

Using various scaling arguments we have gleaned from our simple model a series of non-dimensional numbers characteristic of droplet bounce apoapses and times of flight, but these dimensionless groups depend on a set of physical parameters. Unfortunately not all of these parameters are physically practical to accurately measure by experiment. Droplet free charge q , in particular, could in principle be directly measured by collecting the charged drops in a faraday cup under low-g and measuring the change in capacitance of the cup using a very high input-resistance electrometer, but this is a problematic experiment to set up in a drop tower from a practical standpoint. The other state variables we can directly measure by experiment with varying levels of accuracy. To measure the charge, q , we instead turn to parameter estimation techniques. Our work flow to identify this parameter is as follows:

1. Experimentally vary V_d , σ and capture droplet trajectories using a high-speed camera.

2. Digitize droplet trajectories by using automatic tracking of ellipse-fitted centers of mass on the thresholded video.
3. Slice droplet trajectories by their bounce minima, and apply a smoothing filter.
4. Extract the droplet charge (and other experimental parameters) by maximizing the log-likelihood of the data given the dynamical model and parameters, by varying the parameter vector using a direct search optimization.

Mathematically we state that we find the parameters \mathbf{x} that solve the inverse problem $G(\mathbf{x}) = \mathbf{d}$, using a direct search method (*Nelder-Mead*).

$$\min \chi^2 = \min \sum_{i=1}^n \frac{(y_d(t)_i - y_G(t, \mathbf{x})_i)^2}{y_G(t, \mathbf{x})_i}$$

$$\mathbf{x} = \begin{cases} q \\ V_d \\ \sigma \end{cases} \text{ subject to constraints } g = \begin{cases} V_d \pm u_{exp} \\ \sigma \pm u_{exp} \\ y_0 \pm u_{exp} \\ t_0 \pm u_{exp} \end{cases}$$

where $y_G(t, \mathbf{x})$ is a numerical solution of the equation of motion

$$my'' = \frac{1}{2}\rho C_D A_d y'^2 + qE(y) + Kq^2 y^{-2}$$

3.4.1 Inverse Problems

Suppose we have a model $G(\mathbf{x})$, with a vector of parameters \mathbf{x} , and set of (noiseless) observations \mathbf{d} , then we naturally expect there to exist a relationship

$$G(\mathbf{x}) = \mathbf{d},$$

where the operator G might be an ODE. Suppose the model $G(\mathbf{x})$ is the ODE

$$y'(t) = f(t, \mathbf{y}; \mathbf{x}), \mathbf{y} \in \mathbb{R}^n,$$

and a collection of n measurements of experimental data

$$\mathbf{d} = (t_1, \mathbf{y}_1), (t_2, \mathbf{y}_2), \dots, (t_k, \mathbf{y}_k).$$

The process of fitting a function, defined by a collection of parameters, to a data set is called the discrete inverse, or parameter estimation problem (as opposed to the *forward problem* to find \mathbf{d} given \mathbf{x} and $G(\mathbf{x})$). This is a familiar procedure when the determination of model parameters is done using linear or polynomial regression. However there are approaches even to fitting an arbitrary function to a noisy and sparse dataset. In this work we use the conventional Maximum Likelihood Estimate (MLE) method to identify the model parameters.

Using MLE we don't ask the question: "what is the probability that my set of model parameters is correct?" (because the probability is very nearly zero!), but rather "given my set of model parameters, what is the probability that this data set occurred (what is the likelihood of the parameters given

the data)?"'. Bayes' Theorem holds that

$$\text{prob}(X|D, I) = \frac{\text{prob}(D|X, I) \times \text{prob}(X|I)}{\text{prob}(D|I)}$$

where D are our observations (dataset), X is our vector of parameters, and I is general background information about the problem including our mathematical model (for instance the ODE above), and

$\text{prob}(X D, I)$	posterior probability density function,
$\text{prob}(D X, I)$	likelihood function,
$\text{prob}(X I)$	prior probability density function,
$\text{prob}(D I)$	evidence.

The posterior probability density function (PDF) $\text{prob}(X|D, I)$, is ultimately what we want to estimate, the prior PDF $\text{prob}(X|I)$, reflects our knowledge of the system, and the evidence $\text{prob}(D|I)$, is the likelihood of the data based on our knowledge. We also note that since it only makes sense to compare the conditional PDF's for the same data, we can ignore the denominator (that is, the evidence). We further note that the prior $\text{prob}(X|I)$, is fixed before our observations and so can be treated as invariant to our problem. We can therefore infer that $\text{prob}(X|D, I) \propto \text{prob}(D|X, I)$. The MLE for the the model parameters \mathbf{x}_0 , then is given by the maximum of the posterior PDF, which is equivalent to the solution of the ODE given the the parameters \mathbf{x} , that produces the highest probability of the observed data. Since the likelihood $\mathcal{L}(\mathbf{x}) = \prod_i^n \mathcal{P}_i$, and the probability \mathcal{P} , of any single observation is less than one, then the total likelihood which is the product of a large number

of probabilities tends to be vanishingly small. The more well behaved log-likelihood is given by

$$\mathcal{M} = \ln(\mathcal{L}) = \ln(\text{prob}(D|X, I)) = \text{const} - \frac{\chi^2}{2}$$

where

$$\chi^2 = \sum_{i=1}^n \frac{(y_d - y_G)_i^2}{\sigma_{d_i}^2}$$

is the χ^2 goodness-of-fit, $y_d = y_d(t)$ is a observation of droplet position at a point in time, and $y_G = y_G(t, \mathbf{x})$ is the droplet position predicted by the solution to the equation of motion at time t , and σ is the standard error of the position measurement. If the number of data points n , is small was can use the Poisson error $\sigma_d^2 = y_G$. The optimal parameter set is the one with the highest probability of observing the data (the maximum of the posterior PDF) and can be determined by maximizing the log-likelihood \mathcal{M} (or minimizing χ^2) of the data \mathbf{d} with respect to the parameter set \mathbf{x} . Thus parameter estimation is a variety of optimization problem.

3.4.2 Smoothing

All optimization methods, whether explicitly or implicitly, follow gradients towards an optimum. In a parameter estimation problem, if we approximate these gradients by finite differences, then the noise manifests itself as amplification of the roughness in the hyper-response surface. Gradient based optimizers do poorly in these situations because they tend to converge to local minima. While so called gradient free algorithms offer an improvement

in this regard, speed of convergence and the quality of the MLE is improved by smoothing the objective function. This is equivalent to smoothing the underlying dataset.

Our choice of smoothing approach depends principally on the nature of the errors in the dataset. The sources of error include misalignment of the camera, error in the fiduciary length scale, perspective due to objects (subject or reference scale) being out of the photographic plane, and various errors arising in the digitization process (including the difference between the thresholded ellipse fitted centroid and the true centroid of the non-ellipse drop centroid). Some of these errors are systematic in origin and introduce consistent biases into the data (e.g. coherent spectral sources, rather than truly stochastic noise). Data smoothing does little to help systematic errors in that they are usually of lower frequency than the signal. Random errors, by contrast, are assumed to have a Gaussian distribution (by the central limit theorem), and are independent of the signal (which inherently results from a deterministic process).

We experimented with a variety of filters implemented in the `scipy.signal` Python *SciPy* [52] module on a representative set of trajectory data; these methods include 1D Gaussian convolution, Wiener, Butterworth, and Savitsky-Golay filters. Qualitatively comparing these smoothing methods (by hand tuning filter orders and window sizes) we find that we loose too many data points in the smoothing process, large amplitudes are overly smoothed by repeated filtering passes, or there are significant end effects for most of these methods. A comparison of these smoothing approaches on a representative trajectory data set is shown in Figure 3.7.

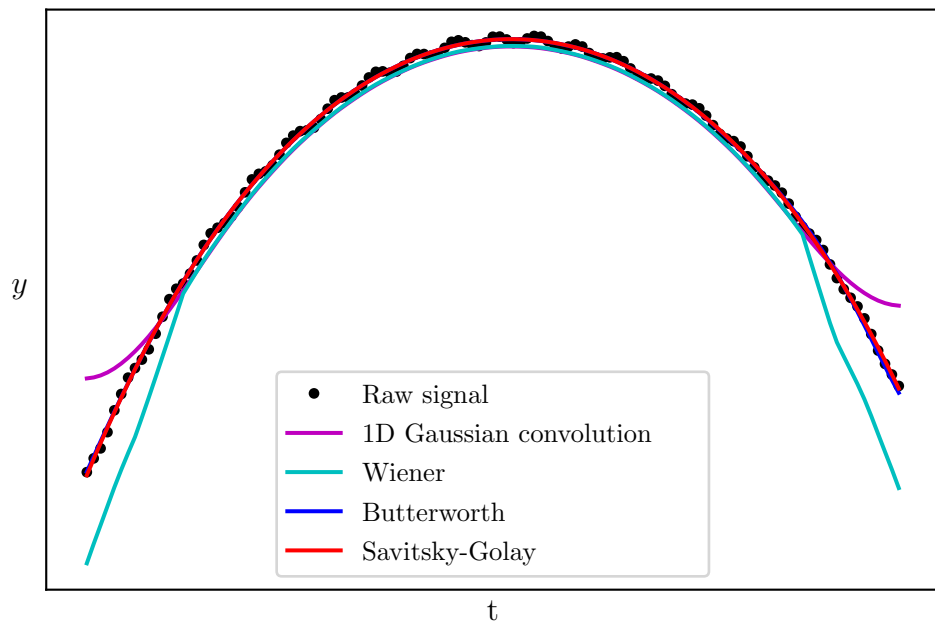


Figure 3.7: The underlying signal is ‘noisy’, due partially to deterministic errors in determining the center of mass position. These deterministic errors are largely due to droplet oscillations, especially the rapidly damped higher harmonics which do not have azimuthal symmetry. There is also Gaussian error in the ellipse fitting due to thresholding and noise in the video itself. We see that 1D Gaussian convolution and Wiener filters suffer from significant end effects. At this scale Butterworth and Savitsky-Golay filters are nearly indistinguishable.

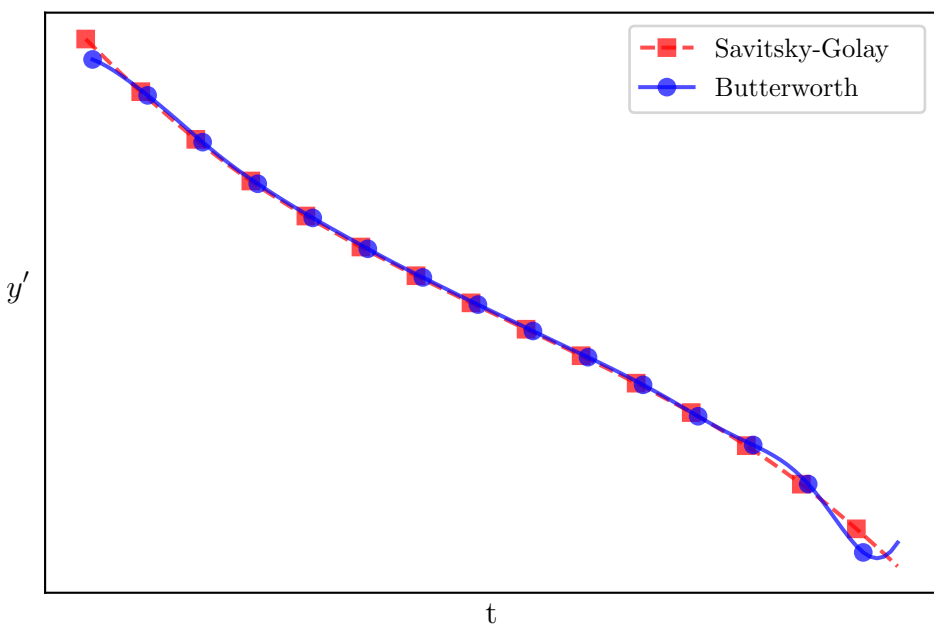


Figure 3.8: Comparing the first derivatives of the Butterworth and Savitsky-Golay filters we see that the Butterworth filter also suffers from a slight end effect. This implies that the optimization will find a different optima of the likelihood depending on which type of filter is used.

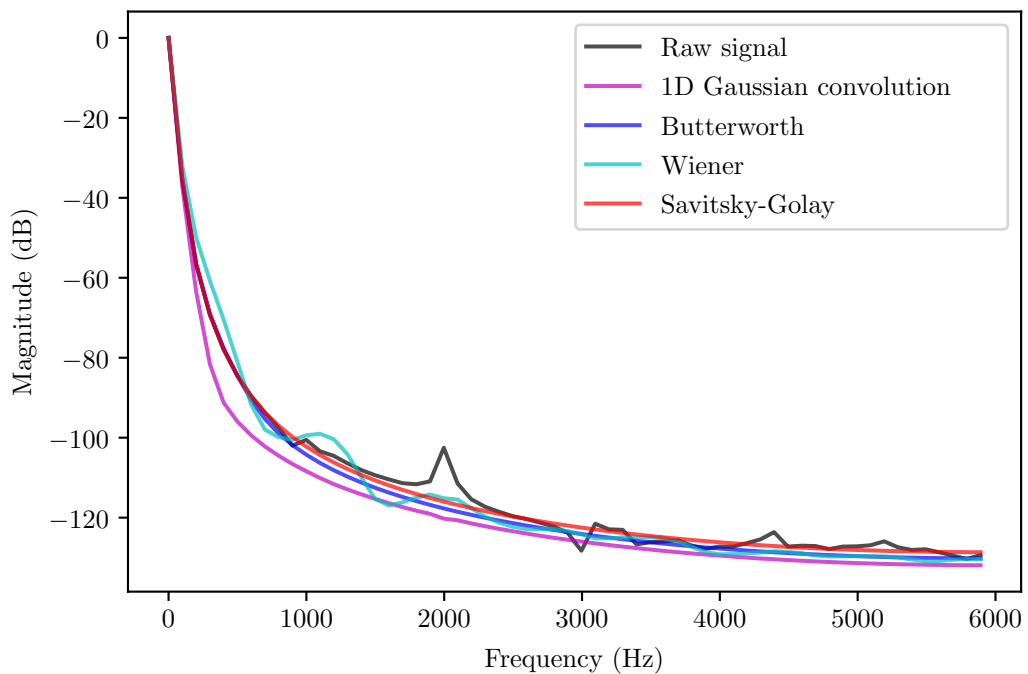


Figure 3.9: The power spectra has a peak at 1 Hz, which is the droplet trajectory parabola itself, and smaller peaks in the kHz range corresponding to various noise frequencies. The Savitsky-Golay and Butterworth filters seem to have the least distortion of the power spectra of the true signal. Both also do a good job of attenuating the noise at the 2 kHz peak.

The Savitsky-Golay, and Butterworth filters both produce fairly smooth derivatives as can be seen in Figure 3.8; but the small window-size needed for Butterworth filter tends to also produce a noticeable end effect. The Savitsky-Golay filter essentially uses a moving-window based on local least-squares polynomial approximations. It was shown that fitting a polynomial to a set of input samples and then evaluating the resulting polynomial at a single point within the approximation interval is equivalent to discrete convolution with a fixed impulse response [53]. A beneficial property of this kind of low-pass filter is their tendency to maintain waveform amplitudes, and so they are attractive in applications having noisy signals with sharply pointed waveforms such as ultrasound or synthetic aperture radar [54]. Because Savitsky-Golay is a Finite Impulse Response (FIR) filter it requires data points to be equally spaced; to accommodate this requirement we interpolate points between the small gaps which sometime occur in the tracking results from image analysis. We use a moving window size slightly smaller than the length of the current bounce in a single drop jump data set. The windows are piecewise defined by partitioning the data set into a series of individual bounces (the dataset is sliced at minima identified after an initial rough smoothing pass, using the `scipy.signal.argrelextrema()` function). The Savitsky-Golay polynomial order is 4.

To understand how these filters differ it is useful to look at their frequency response. In Fourier space, convolution becomes a multiplication, and we can understand what a filter does by looking at which frequencies it lets pass through. We can do this using a Discrete Fourier Transform (though it is worth noting that our signal is not truly periodic). The power spectra for

these same data are shown in Figure 3.9.

3.4.3 Optimization

Most generally a constrained optimization problem is stated as

minimize: $f(\mathbf{x})$ objective function

subject to:

$g_j(\mathbf{x}) \leq 0$ inequality constraints

$h_k(\mathbf{x}) = 0$ equality constraints

$$\text{where } \mathbf{x} = \begin{cases} x_1 \\ x_2 \\ \vdots \\ x_n \end{cases} \quad \text{design variables}$$

Mathematical optimization is the problem of finding minima of a function f . In this context the function is called the cost, or objective function. The field of mathematical optimization is as old as calculus itself, and the number of particular optimization techniques is correspondingly myriad; particular techniques lend themselves well to particular types of optimization problems. The minima of the objective function f is sought on a domain A specified by the constraints of the problem; this domain is usually called the feasible region. Minima of objective function $f : A \rightarrow \mathbb{R}^m$ are called feasible solutions. If the function f is convex the feasible solution is the global minimum, otherwise additional local minima exist. The scale of the optimization problem is set ultimately by dimensionality of the objective

function. Functions may not always be smooth in the sense of having continuous derivatives, and this is problematic in that optimization methods fundamentally rely on gradients of the objective function. Problems with anisotropic objective functions where there is strong covariance between the parameters, and the gradient vector generally tends to differ significantly from the Newton direction ($-\mathbf{H}^{-1}f'(\mathbf{x})^T$, where \mathbf{H} is the Hessian matrix) are considered ill-conditioned. Ill-conditioned problems gradient based deterministic search tend to converge slowly as they take a zigzagging path determined by the local value of the gradient rather than following the Newton-direction vector which towards the minimum. Numerical optimization may deal with black box functions (where we do not have an explicit mathematical expression of the function we are optimizing). Black box problems are challenging because we do not have access to analytic gradients of the objective function, and approximating them by finite-differences is slow and noisy. In general, noisy, black box, non-linear, non-quadratic, non-convex, constrained, ill-conditioned, high-dimensional objective functions are problematic to optimize. Unfortunately, problems of this type are the essence of the parameter estimation, which often leads to its characterization as an ‘art’ rather than a precise science (though we submit that it is a dark art).

The equation of motion behaves stiffly due to the large disparity in Coulombic, image charge length scales. We integrate it numerically using the `odeint` *Scipy* module. This is a shake-and-bake Python wrapper for the venerable 1982 *netlib ODEPACK* library double-precision `lsoda` (Livermore Solver for Ordinary Differential equations with Automatic method switching for stiff and nonstiff problems) integrator [55]. The function switches

between Adams (nonstiff) and Backwards Differentiation Formulas (BDF, stiff) according to the dynamic value of a set of stiffness eigenvalues.

Our specific optimization problem is non-convex, mixed discrete-continuous black-box (noisy), and highly ill-conditioned which is essentially the worst case scenario for an optimization problem. The ill-conditioning arises due to the strong covariance between several of the model parameters (particularly $q = q(V_d, E_0)$). The non-convexity of the problem implies that there are many local minima of the objective function. While in principle a gradient-based optimizer (for instance using the quasi-Newton method of Broyden, Fletcher, Goldfarb, and Shanno (BFGS) [56]) could be used by using finite-differences to obtain approximate gradients of the χ^2 objective function, in practice doing so is extremely problematic because the noise-to-signal ratio of the objective function scales like $\mathcal{O}(f)$ for $\frac{df}{dt}$ and $\mathcal{O}(f^2)$ for $\frac{d^2f}{dt^2}$ which will tend to cause convergence to a local minima which is only an artifact of the likelihood response surface [57]. As a further practical matter, given the relatively expensive function-calls (which requires solving a stiff, non-linear ODE) gradient-free approaches tend to offer better performance regardless [58].

We use a gradient-free, direct-search approach: Nelder-Mead [59] implemented in `scipy.optimize`. Nelder-Mead is robust to noise (relatively speaking), and is thrifty with our extremely expensive function-calls. *Nelder-Mead*, sometimes called simplex-search or downhill-simplex, is a heuristic search method, with no guarantee of optimal solutions, but is well-established and widely used despite that. *Nelder-Mead* is based on the concept of a N -simplex, which generalizes a triangle into higher dimensions as a polytrope

of $N + 1$ vertices in N dimensions. It uses only-function calls and expands or contracts the simplex according to the function values at its vertices in a way visually reminiscent (in \mathbb{R}^3) of the oscillations of the jumping droplets themselves (in fact *Nelder-Mead* is sometimes also called the “amoeba method”). Very little is known about the convergence properties of the *Nelder-Mead* algorithm in its classical form for non-smooth objective functions [60], except that in general it doesn’t satisfy the properties required for convergence by other direct search algorithms: that the simplex remains uniformly non-degenerate, and that some form of “sufficient” descent condition for function values at the vertices is required at each iteration. Scaling can help solve convergence problems and improve numerical stability. We precondition the optimization problem by minimizing $\ln(\chi^2)$, and using a naive scaling (scaling variables such that their magnitudes $\sim \mathcal{O}(1)$) of our constraints by their initial guesses. Here is goal is to make the problem equally sensitive to steps in any direction. *Nelder-Mead* is not a global optimizer, though there are variants which use sequential local searches with probabilistic restarts to achieve globality. However global optimization usually comes at a tremendous computational cost. However, *Nelder-Mead* behaves less locally than many gradient-based approaches. The convergence history of the parameter MLE using *Nelder-Mead* for a single drop jump experiment is shown in Figure 3.10. Results of the parameter estimation are shown in Figures 3.11, 3.12.

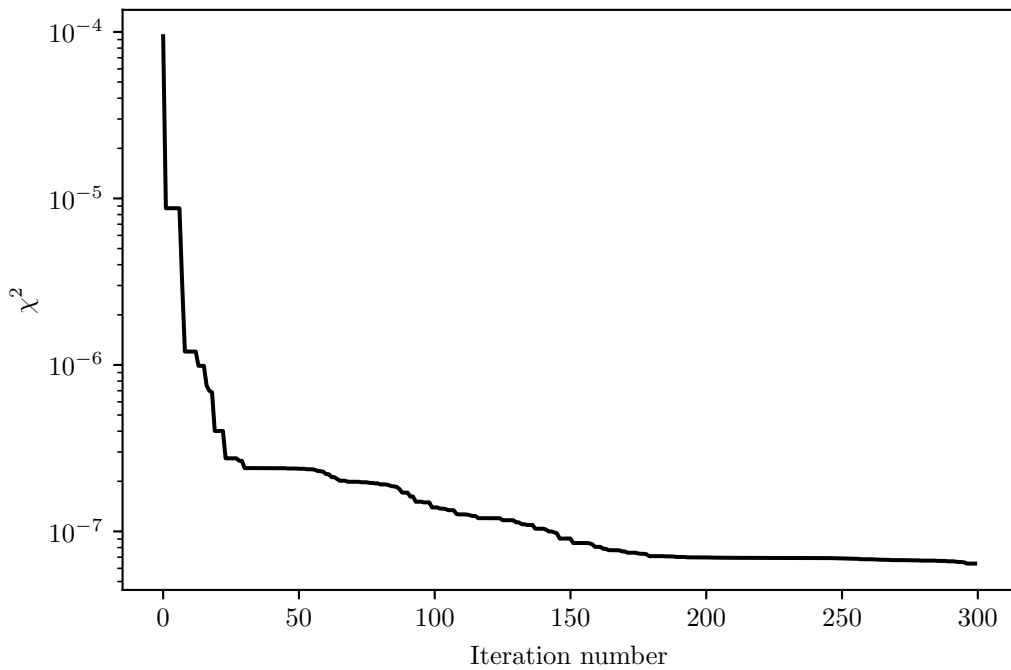


Figure 3.10: As is typical with *Nelder-Mead* much of the improvement in χ^2 is realized in the first few iterations. Overall the rate of convergence is sub-linear, which is to be expected for non-linear constrained problems using an heuristic algorithm.

3.4.4 Identifiability

That we are capable of fitting any arbitrary model to a dataset given sufficient degrees of freedom in our parameters is admittedly a disconcerting issue, begging the question “given the structure of the model is it possible to uniquely estimate the unknown parameters?” This question is called the problem of identifiability. However, some of the inverse model parameters are constrained by our experimental observations of them and their associated measurement uncertainties. This, we hope, makes the specter of an over fit model less frightening, but does convert our unconstrained optimization problem to an constrained one which raises special difficulties of its own,

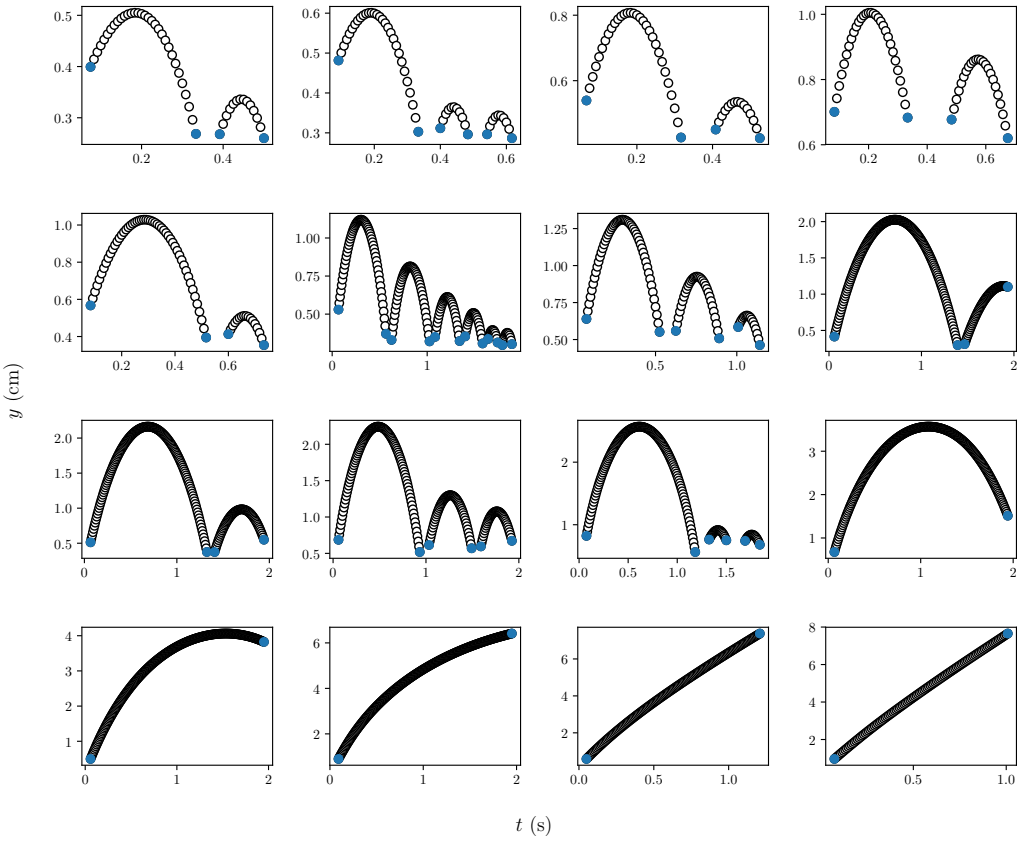


Figure 3.11: A series of filtered droplet trajectories arranged by increasing apoapse. The blue dots represent either the beginning and end of the experiment, or points at which the droplet is either coming into, or leaving contact with the surface.

which we discuss below.

The *Nelder-Mead* direct search method cannot be used with explicitly constrained problems. However, there are various implicit approaches to (approximately) solving general constrained problems using unconstrained algorithms. Generally, this is achieved by domain transformations or the use of penalty functions. By the addition of a penalty function which depends in some way on the values of the constraints to the objective function, we minimize a pseudo-objective function where the infeasibility of the constraints

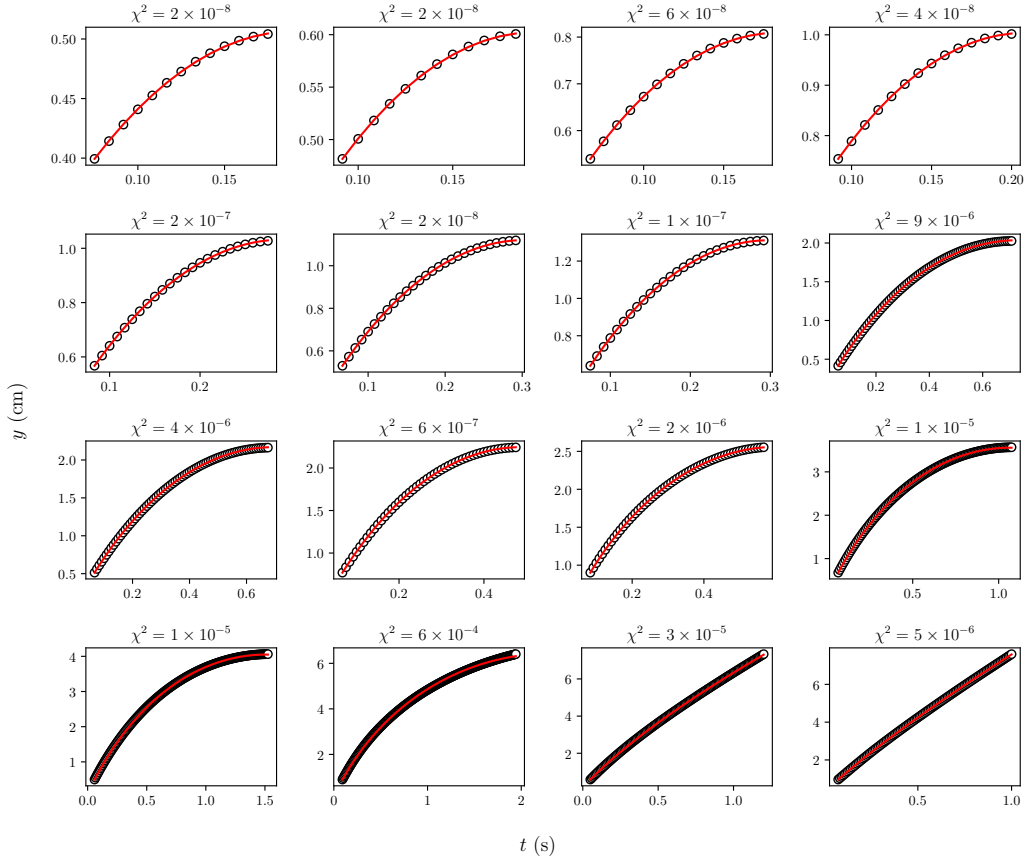


Figure 3.12: A series of droplet trajectories showing the results of the parameter estimation. The trajectories are shown only up to the apoapse of the first bounce. The red lines show the ODE solution with given the MLE parameter vector. χ^2 goodness-of-fit varies between 1×10^{-5} and 1×10^{-8} with the better fit occurring typically for the droplets with the lowest apoapses.

is minimized simultaneously to the objective function.

There are various penalty function schemes. We use an Exterior Penalty Function as a simple way of converting the constrained problem into an unconstrained one. These are especially useful in cases where the constraints are not “hard” in the sense that they need to be satisfied precisely. General penalty functions, which are sequential unconstrained minimization techniques, reformulate the general constrained problem as the

pseudo-objective function given by

$$\phi(\mathbf{x}, r_p) = F(\mathbf{x}) + r_p P(\mathbf{x})$$

where $P(\mathbf{x})$ the penalty function, is given by

$$P(\mathbf{x}) = \sum_{j=1}^m \{\max[0, g_j(\mathbf{x})]\}^2 + \sum_{k=1}^l [h_k(\mathbf{x})]^2. \quad (3.1)$$

We see from Equation 3.1 that there is no penalty if the constraints $g_j(\mathbf{x})$, and $h_k(\mathbf{x})$ are satisfied.

The Exterior Penalty Function specifically (and all Penalty Function approaches in general) do have several drawbacks. Namely these include the possibility of the objective function being undefined outside of the set of feasible solutions. Additionally, by naively “encouraging” feasibility of the solution using large values of the penalty parameter, r_p , we will tend to ill-condition the unconstrained formulation of the problem (though in our implementation the preconditioning tends to make the pseudo-objective function less and less sensitive to the constraints as the likelihood is approaches a maximum). We use the measured values of u_0 , V_d , and E_0 , and the informed guess $q \approx kV_d^{2/3}E_0$ where k is a constant $k \approx 1^{-11}$ as an initial guess for the parameter vector \mathbf{x} . We stop the optimization after 300 iterations rather than waiting for convergence.

We’re interested in the variance and co-variance as a means to determine the quality if the parameter estimate. The (i, j) -th element of the matrix $\sigma(\mathbf{x}, \mathbf{y})$ is equal to the covariance $\text{cov}(X_i, Y_j)$ between the i -th scalar compo-

ment of \mathbf{x} and the j -th scalar component of \mathbf{y} . Here the concept of error bars in linear correlation associated with a covariance matrix are not suitable. We might try to generalize the idea of confidence intervals to a multidimensional space, but it is likely difficult to describe the surface of the (smallest) hyper-volume containing 90% of the probability with just a few numbers. The situation becomes worse if the probability density function has several maxima. However, there is another approach to find the covariance matrix [ref]

$$[\sigma^2]_{ij} = - \left[(\nabla^2 \mathcal{L})^{-1} \right]_{ij} = 2 [\nabla^2 (\chi^2)]_{ij}^{-1} = - [H^{-1}]_{ij}$$

where H refers to the Hessian matrix and $[\sigma^2]_{ij}$ is the covariance matrix C . The issue of identifiability is especially fraught for non-linear, black box type problems were it is difficult to explicitly evaluate the Hessian. The likelihood function (and thus the posterior probability density function) are defined completely by the optimal solution \mathbf{x} and the second derivative of \mathcal{L} at the maximum, which corresponds to the covariance matrix C . The standard errors (marginal variances) are the square roots of the diagonal of the covariance matrix. The Hessian matrix must be negative definite for \mathcal{L} to have a maximum at \mathbf{x}_0 . We obtain an approximate Hessian using the approach suggested in Nelder's original paper, by fitting quadratics to the simplex vertices and midpoints [59][61]. We can use the condition number

$$\text{cond}(H) = \frac{\max[\text{eig}(H)]}{\min[\text{eig}(H)]}$$

to make a qualitative assesment of the stability of the problem. We find typical condition numbers $\sim \mathcal{O}(10^{27})$. In fact, in many cases our Hessian is not

negative definite, or invertible at the minima \mathbf{x}_0 , which implies negative values of the variances (which is impossible). These issues indicate the problem is extremely ill-conditioned near the minima \mathbf{x}_0 . Given that the parameter estimates are highly colinear, it is unsurprising that the Hessian matrix is near-singular and its inversion is either impossible or involves significant numerical error. Posteriori verification of the results is crucial to bound the identifiability of the parameter estimation problem, but it remains as future work. Several sources suggest sensitivity analysis of the parameter estimates by generation of synthetic Monte Carlo data sets as a means of establishing identifiability [62][63].

Chapter 4

Results

4.1 Charge Estimates

We found the distribution of mostly likely experimental net charges for a population of the droplets jumped in low-gravity. A covariance plot of the model variables is shown in Figure 4.1. The multicollinear dependence of charge on droplet surface area, A , and the characteristic electric field, E_0 , is evident. Assuming the main effect is the interaction between charge and electric field, a Robust Least Squares model fit $q \sim kAE_0$ (using the Python `statsmodels.formula.api.RLM` function), with the non-linear transformation $A = V_d^{2/3}$, found that $k = 5.01 \times 10^{-11} \pm 2.85 \times 10^{-11}$ with $R^2 = 0.946$. This model uses Huber's T norm, median absolute scaling, and H1 covariance estimation. A contour plot showing the estimated droplet free charge as a function of V_d and φ_s is shown in Figure 4.2.

A two-ways T-test comparison of charge distributions between the droplet bounce experiment and a corollary experiment with zero electric field at the

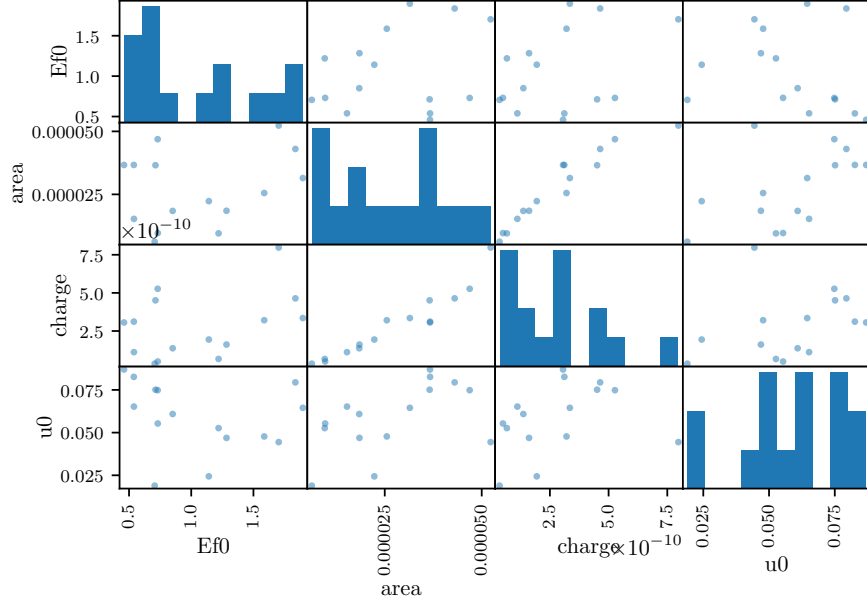


Figure 4.1: A simple EMA plot.

time of droplet deposition on the superhydrophobic surface suggests that the droplet charge is induced by the electric field, rather than through contact charging on the PTFE layer ($t = 5.11, p = 0.0002$). The T-test informs us that the charge distribution are about 5 times more different from each other as they are within each other, and there is a 0.02% probability that this result happened by chance. This corollary experiment is documented in Appendix A.

The model $q \sim kAE_0$ is incidentally very similar to the classical solution for the surface charge density of a half-spherical conductor with a field

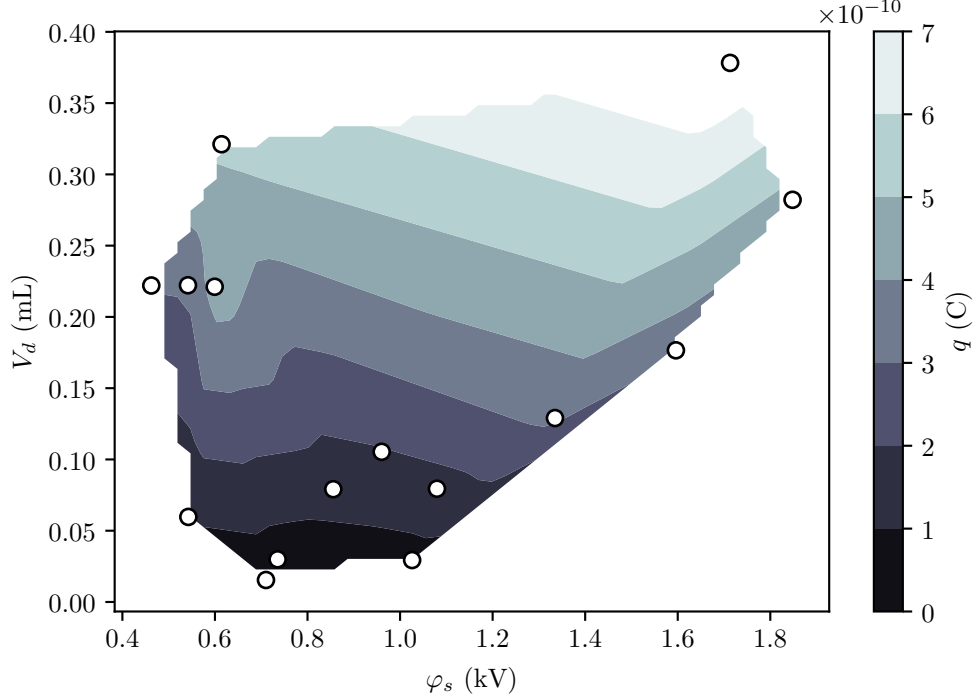


Figure 4.2: A simple EMA plot.

induced dipole [36]

$$\begin{aligned}
 q &= 3\epsilon_0 E_0 \int_A \cos \theta dA \\
 &= 3\pi^{1/3} 6 (6V_d)^{2/3} \epsilon_0 E_0 \int_{\pi/2}^{4\pi/2} \cos \theta d\theta \\
 &= kE_0 V_d^{2/3}
 \end{aligned}$$

with $k \approx 1.3 \times 10^{-10}$. This is also of a similar form to the charge found by Takamatsu and coauthors for droplets falling from a grounded nozzle in an external electric field [64]

$$q = 4\pi\epsilon_0\beta E_0 R_d^2$$

with $\beta \approx 2.63$.

4.2 Scale Quantities

The dielectrophoretic force plays a very small role when droplets have net charge in a DC field; the condition to neglect the DEP force was satisfied for all experiments in the dataset. Dimensional droplet apoapses scale closely with $\mathbb{E}u$ as seen in Figure 4.3. The relative magnitudes of the simulated forces felt by the droplets is shown in Figure 4.4. Forces acting on the drops vary in magnitude between $\mathcal{O}(10^{-6}) - \mathcal{O}(10^{-4})$ N. We see that, of the drops in the experimental dataset only the two with the largest $\mathbb{E}u$, $\mathbb{E}u \sim \mathcal{O}(1)$ could appropriately be said to be in the inertial electro-viscous regime. In all other cases image forces are much stronger than drag. For these drops $\mathbb{E}u \gg 1/8\pi$, and are likely on escape trajectories. The image forces themselves rapidly become small compared to Coulomb forces for drops with apoapses $\max(y) \gtrapprox L$, thus it is reasonable to claim that for intermediate drops Coulomb force scales as inertia, and we can neglect the effects of drag and image forces.

In the non-dimensional trajectories with short-time scaling shown in Figure 4.5, we see that the trajectory apoapses are consistently $\mathcal{O}(1)$, but most trajectories overshoot their characteristic time scale (which predicts returns at $\bar{t} = 2$ to the first order). We also observe that that $\mathbb{E}u$ is not typically a small number in this regime, imperiling our use of asymptotic estimates in this regime. We can perhaps gain some insight by comparing the asymptotic estimate for return times to the scaled experimental return times. We see in Figure 4.6 that the long-time scaled non-dimensional time of first bounce in the experiment t_b/t_c , compares poorly to the asymptotic estimate for returns

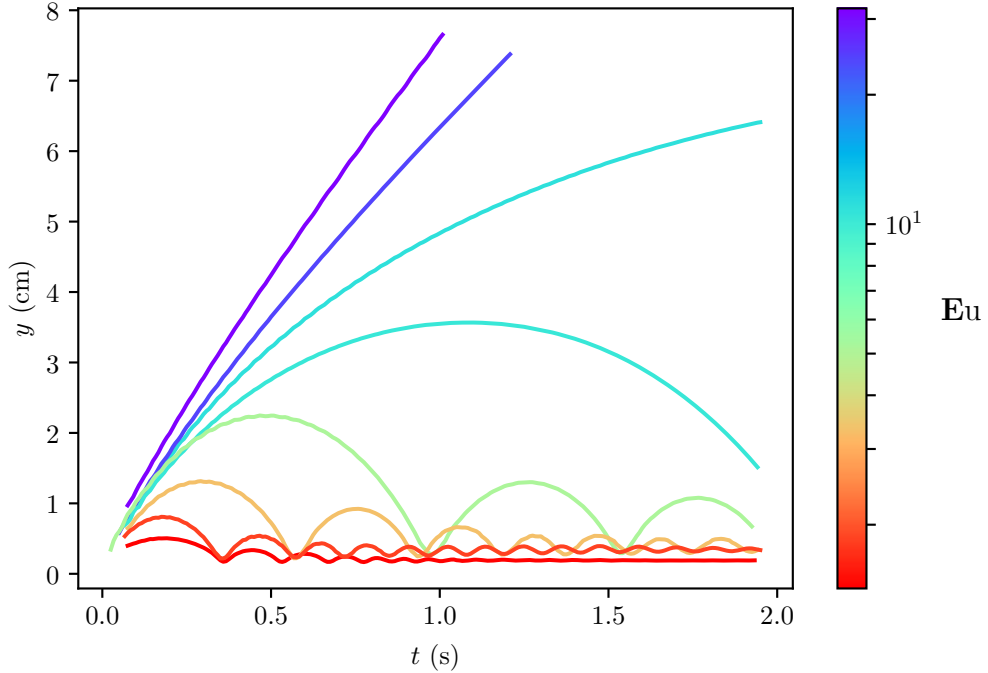


Figure 4.3: Droplet trajectories as a function of Eu .

t_f as Eu_+ becomes large. This is very much as we'd expect, but it is also unfortunate; for small Eu the asymptotic length scale could be used to improve the characteristic length scale by $t_a = t_c t_f$. We also notice a two-tailed effect in the data; for the small Eu droplets, the long-time scaling distorts the return times considerably.

The covariance of Im with Eu is shown in Figure 4.7. Predictably, there is quite strong correlation between the dimensionless groups. We also see that $\text{Im} < 1$ for all drops. Using an OLS regression, we find the model $\text{Im} \sim (0.012 \pm 0.003)\text{Eu} + (0.212 \pm 0.036)$ with $R^2 = 0.59$.

Finally we show several trajectories in the long-time scaled regime in Figure 4.8. We should note that there are several kinds of systematic error that influence our data. We assume that droplet translate purely along the

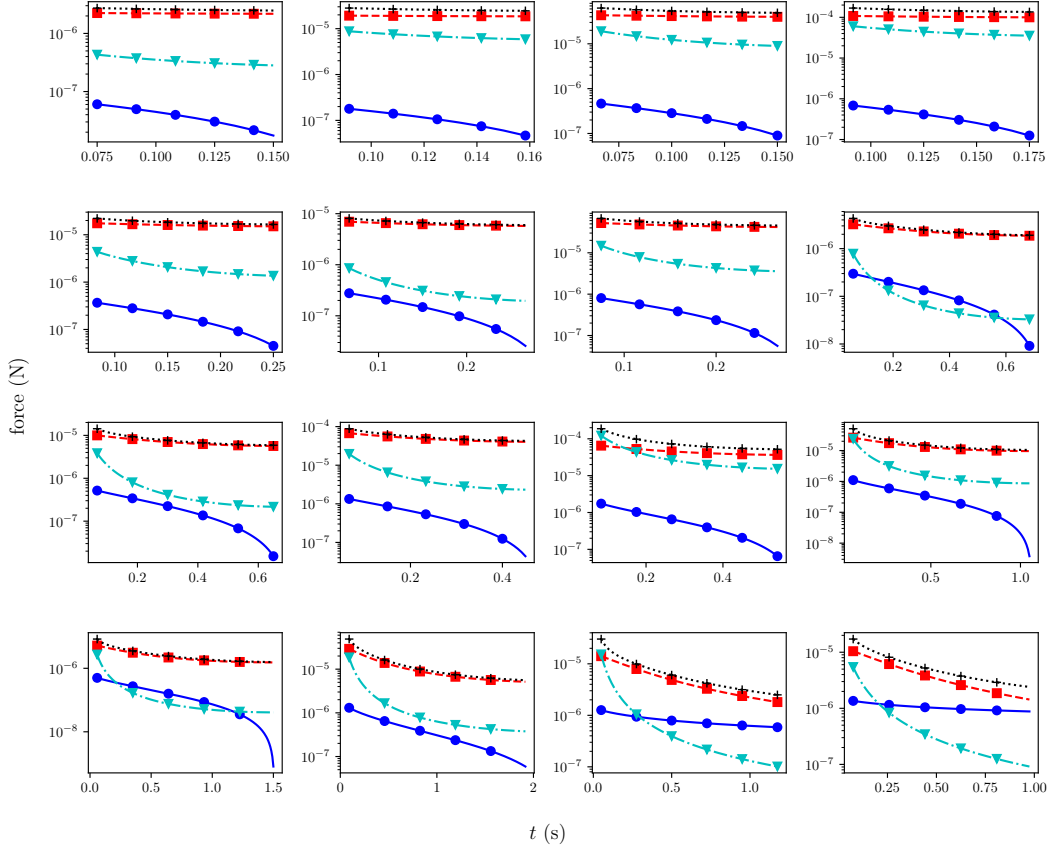


Figure 4.4: Simulated forces acting on the droplet. Experiments are shown by order of increasing apoapse.

central axis of the electric field, but in practice, despite the improvement in surface charge density uniformity produced by corona charging, there are still local areas of especially high charge density. In principle, this kind of error should become small for droplets which are far enough away from the charge distribution, that the geometry of the charge distribution disappears, and the electric field looks like that due to a point charge. Another form of error is in the initial velocity as it appears in \mathbf{E}_0 . Because we usually lose the first few frames of video due to camera shake transients at the start of the low-gravity experiment, we will consistently underestimate U_0 because

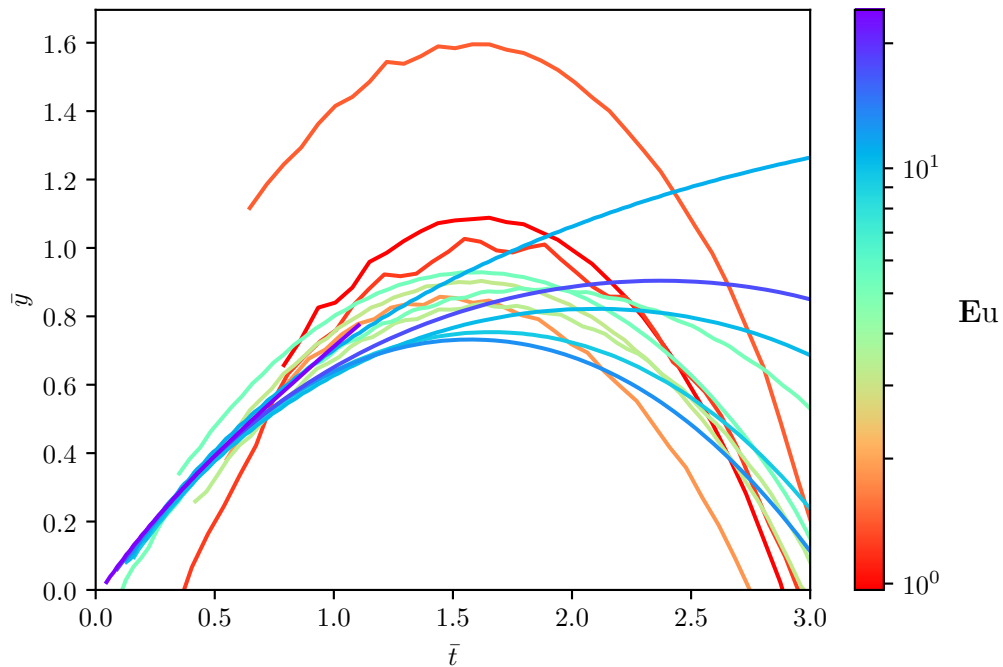


Figure 4.5: Non-dimensional trajectories with the short-time scaling.

the droplet will already have decelerated significantly during that period of time. The primary sources of random error are the effect of contact line hysteresis on the droplet initial velocity, and of the variance in the MLE parameter estimates.

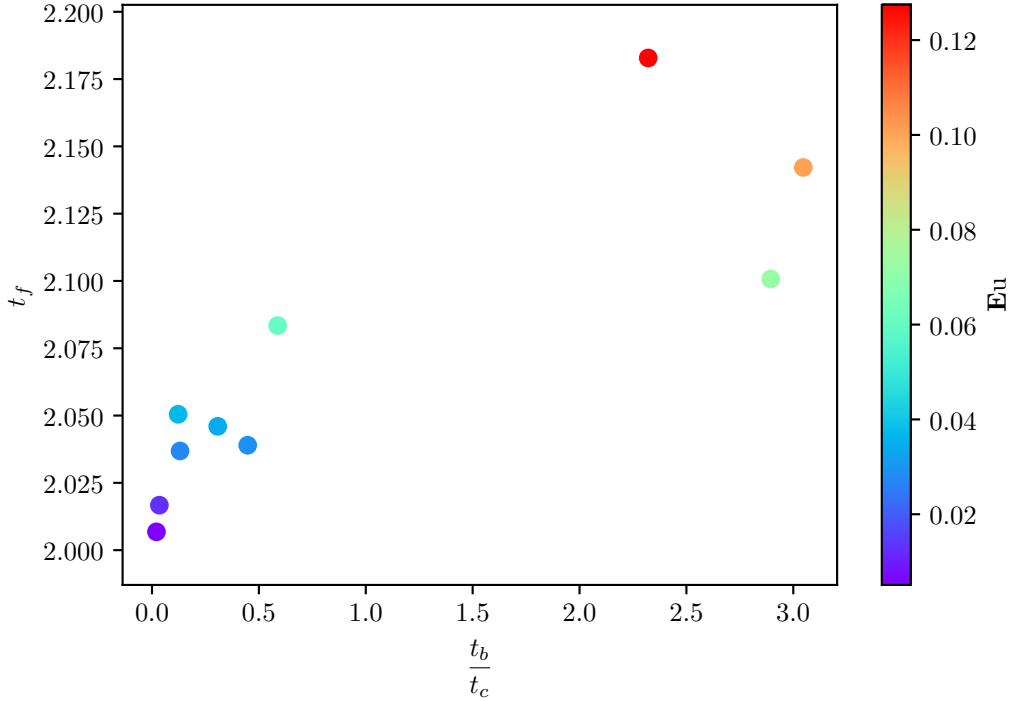


Figure 4.6: .

4.3 Impact Dynamics [placeholder section]

Using the unique capabilities of the low-gravity environment we obtained data on dimensionless contact time and coefficients of restitution at very low Ohnesorge numbers for a range of electric Bond numbers. Despite strong electric fields ($0.5\text{-}1.5\text{ kV/cm}$) we found little evidence for wetting transitions due to exceedance of a critical pressure (the “Fakir impalement”). There is no obvious trend in dimensionless contact time or coefficient of restitution with electric Bond number.

Jump velocities are more strongly damped for relatively small droplet volumes in the presence of the electric fields than was shown by Attari *et al.*. This may be evidence for electrowetting paradoxically enhancing the

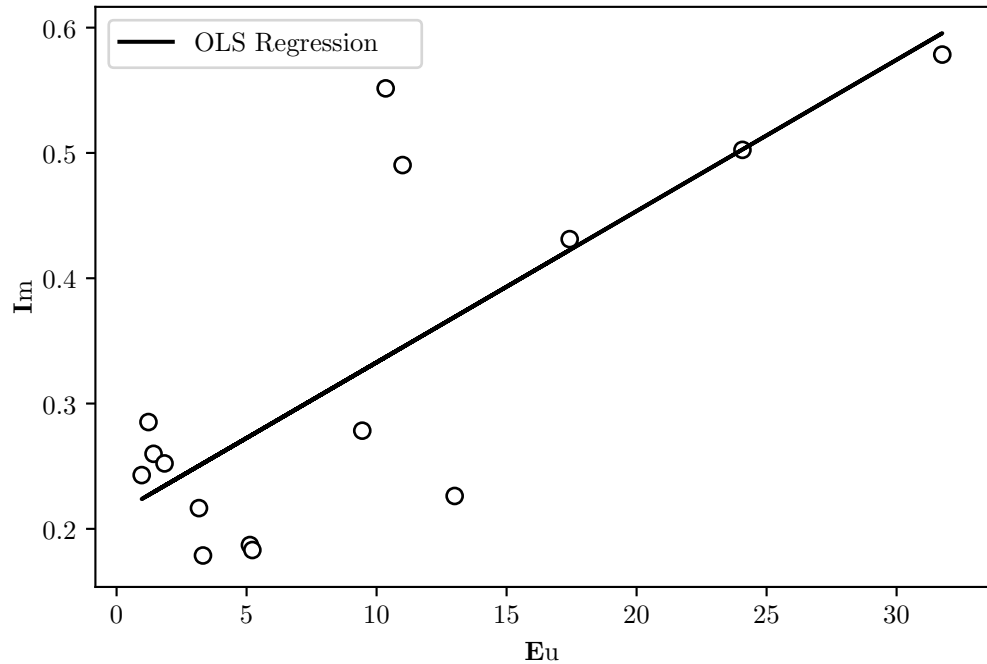


Figure 4.7: .

effect of contact angle hysteresis pinning on sharp corners. (How does this tie into the coefficients of restitution problem?)

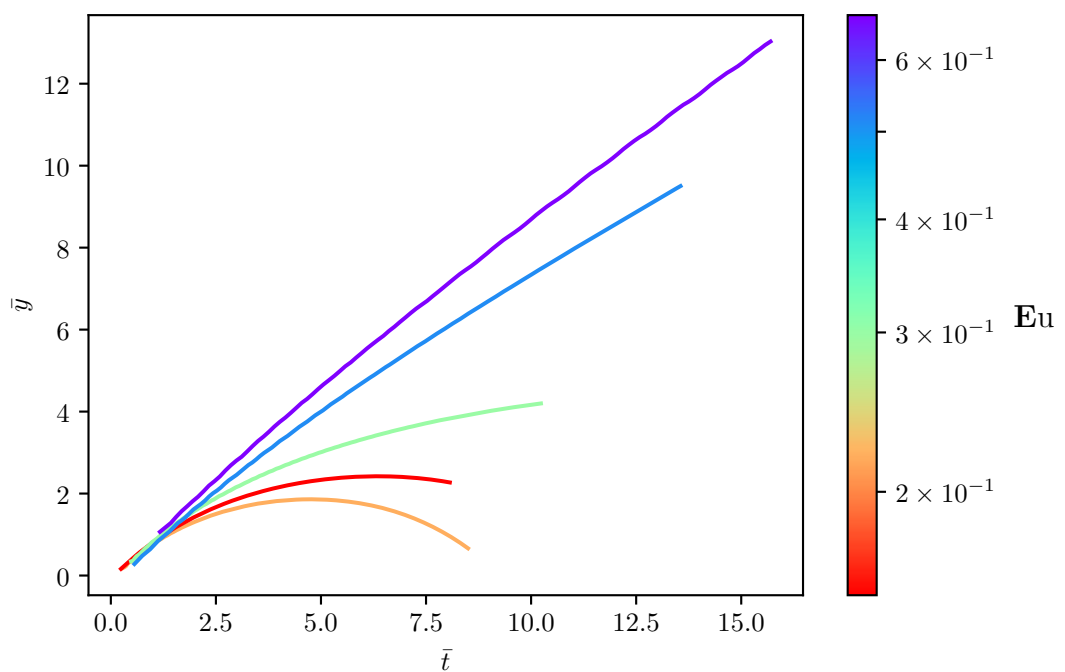


Figure 4.8: Non-dimensional trajectories with the long-time scaling as a function of Eu_+ .

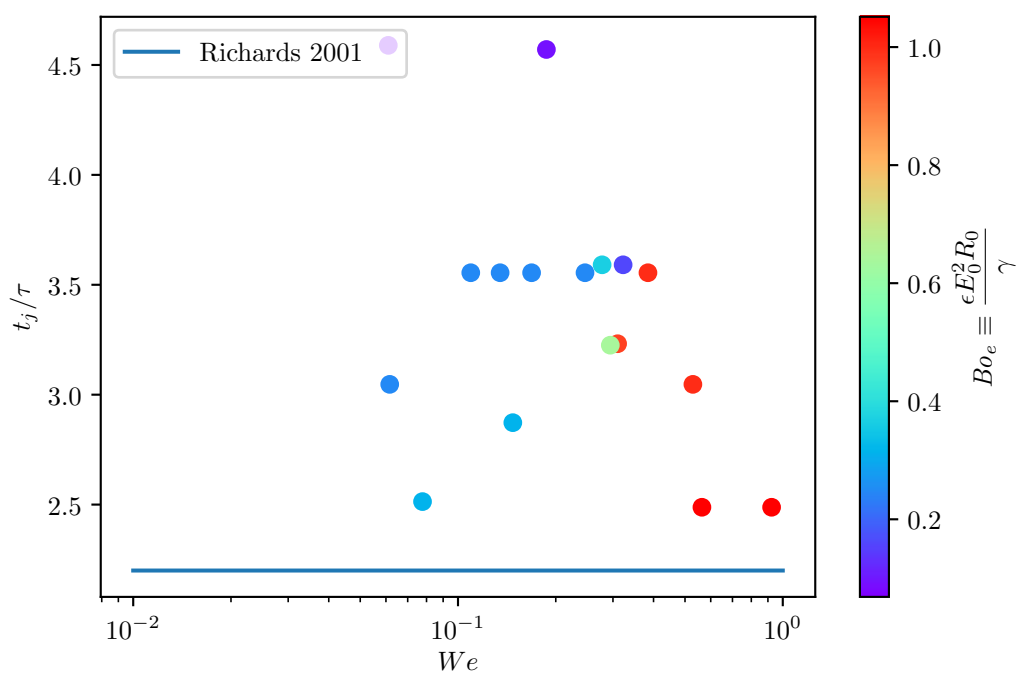


Figure 4.9: .

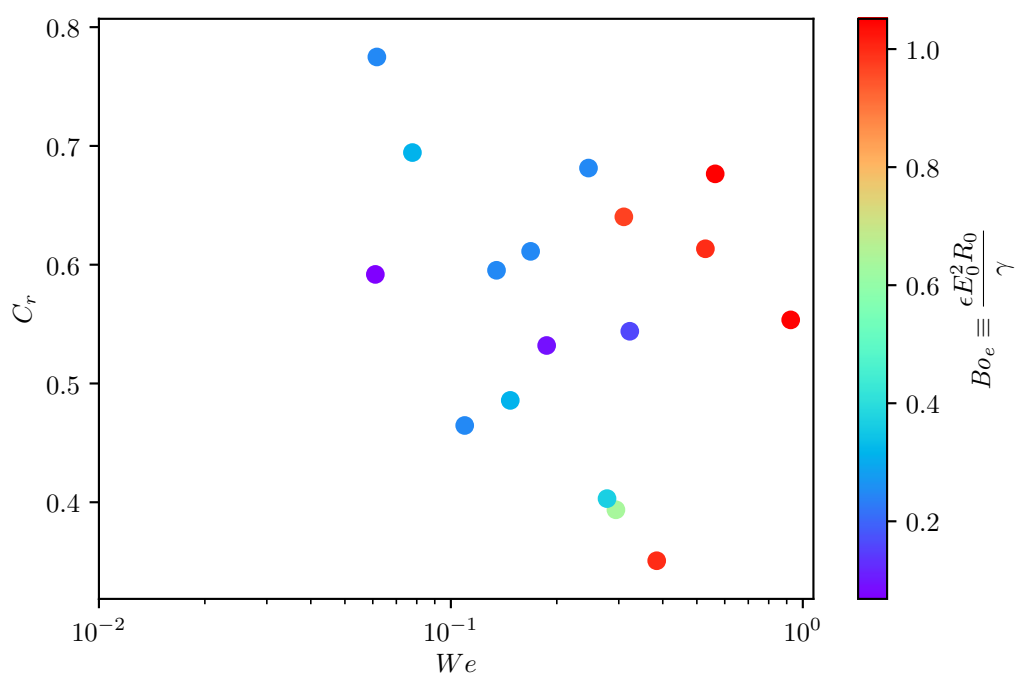


Figure 4.10: .

Appendices

Appendix A

Parallel Plate Method

Since, by the earlier scaling, we presuppose the source of the droplet bouncing behavior to be primarily Coulombic in origin (as opposed to dielectrophoretic), the droplet must have some free charge in addition to the charge induced by the electric field. Whether this free charge arises due to contact charge or field induction To measure this charge concurrent methodologies were used. We determined the droplet free charge by observation of the deflection of the droplets in the region of a known uniform field in a fashion inspired by Millikan's famous experiment to determine the fundamental charge of the electron.

Droplets were jumped in free-fall from a superhydrophobic surface placed between the plates of a parallel plate capacitor of known uniform electric field. The surface was charge neutralized. Since the droplet initial velocity U_0 is parallel to the electric field, the droplets are inertial in the direction of the electric force, and neglecting the effect of image charges mirrored across the conductors, we can determine the magnitude of the droplet charge by a

balance of Coulombic force and inertia given by the equation of motion

$$y'(t) = q\mathbf{E}.$$

Since the drag is negligible in the inertial limit we can find the charge q by fitting a second-order least squares polynomial to the measured droplet positions, equating the t^2 term to the constant acceleration, and dividing by the known, constant magnitude of the electric field.

A 200-880 VAC source with a full wave bridge rectifier circuit was prototyped on perf-board for initial experiments to measure droplet charge. The circuit was analyzed on an laboratory oscilloscope to verify that the AC component of the signal was appropriately small (13 mV at 35 kHz). Current was determined to be a relatively low 80 μ A. The high-voltage source terminals were led to two parallel polished 150x150 mm aluminum plate electrodes. The electrodes were mounted on an insulated 80/20 extruded aluminum rail for ease of adjustment. All droplet charge experiments were conducted with an electrode spacing of 28.30 mm. With this spacing the calibrated electric field between the plates was $\mathbf{E} \approx 35\text{kV/m}$. The electrodes were electrically isolated from the drop rig by two alternating layers of 4 mm thick PMMA sheet and Kapton tape. Potential across the plates was measured periodically with a load-impedance corrected multimeter to account for battery depletion. The typical capacitor rise time of the plates was measured to be 1.4 s, thus to make the most economical use of the brief window a low-gravity a weighted switch was set by hand prior to the drop to close the high-voltage circuit, but which passively safed the system at the resumption of 1-g conditions in the

tower. From a survey of literature we suppose the droplet charge, if they are indeed charged by contact with PTFE, to be some function of the droplet volume and the residence time on the superhydrophobic surface. However, sweeping though droplet volumes over a series of drop tower experiments we find little correlation between droplet volume and free droplet charge.

A brief screening experiment was conducted which alternated the polarity of the field by switching the positive and negative terminal leads between plates. Qualitative observations of droplet electrode preference seem to indicate that the assumption of small polarization stress was well founded. Following this a orthogonal array 3^2 factorial design experiment with two replicates was conducted to test the effect of varying droplet volume and surface stay time on free charge at the time of jumping. It was hypothesized in accordance with previous studies [ref], that free charge would increase for levels of both factors. ANOVA analysis in R of the linear multiple regression model for the data set indicates that neither droplet volume ($p = 0.105$), nor surface stay time ($p = 0.358$) is significant at the 95% confidence level. The overall model F-statistics (2.177 in 2 and 13 degrees of freedom), and coefficients of determination ($r^2 = 0.2509$) indicate that the linear model neither fits the data particularly well, nor does it offer an improvement over the mean model. The mean charge was determined to be positive $2.3 \cdot 10^{-11}$ C, with a standard deviation of $1.8 \cdot 10^{-11}$ C.

Bibliography

- ¹B. J. Motil, J. H. Agui, and F. P. Chiaramonte, “Priorities for microgravity fluid physics research and an overview of gravity-dependent complex fluids research”, (2012).
- ²D. A. Petrash and E. W. Otto, “Controlling the liquid-vapor interface under weightlessness”, *AIAA J* **2**, 56 (1964).
- ³R. M. Jenson, A. P. Wollman, M. M. Weislogel, L. Sharp, R. Green, P. J. Canfield, J. Klatte, and M. E. Dreyer, “Passive phase separation of microgravity bubbly flows using conduit geometry”, *International Journal of Multiphase Flow* **65**, 68–81 (2014).
- ⁴L. J. P. Hastings, “[saturn v/s-IVB stage low gravity fluid mechanics problems and saturn IB liquid hydrogen orbital experiment to verify propellant ullaging and orbital venting system]”, June 1, 1965.
- ⁵J. B. Blackmon, “Collection of liquid propellants in zero gravity with electric fields”, *Journal of Spacecraft and Rockets* **2**, 391–398 (1965).
- ⁶T. J. Snyder, J. B. Schneider, and J. N. Chung, “Dielectrophoresis with application to boiling heat transfer in microgravity. i. numerical analysis”, *Journal of Applied Physics* **89**, 4076–4083 (2001).

- ⁷P. Di Marco, W. Grassi, G. Memoli, T. Takamasa, A. Tomiyama, and S. Hosokawa, “Influence of electric field on single gas-bubble growth and detachment in microgravity”, International Journal of Multiphase Flow **29**, 559–578 (2003).
- ⁸P. D. Marco, “The use of electric force as a replacement of buoyancy in two-phase flow”, Microgravity Science and Technology **24**, 215–228 (2012).
- ⁹T. B. Jones, “Electrohydrodynamic heat pipes”, International Journal of Heat and Mass Transfer **16**, 1045–1048 (1973).
- ¹⁰M. Hurwitz, “Electrohydrodynamic propellant management systems for cryogenic upper stages”, in *3rd annual meeting*, 0 vols., Annual Meeting, DOI: 10.2514/6.1966-922 DOI: 10.2514/6.1966-922 (American Institute of Aeronautics and Astronautics, Nov. 29, 1966).
- ¹¹L. R. Koval and P. G. Bhuta, “Dynamics of a cryogenic liquid in an electric field”, in *Advances in cryogenic engineering: proceedings of the 1966 cryogenic engineering conference university of colorado engineering research center and cryogenics division NBS institute for materials research boulder, colorado june 13–15, 1966*, edited by K. D. Timmerhaus, DOI: 10.1007/978-1-4757-0489-1_10 (Springer US, Boston, MA, 1967), pp. 92–102.
- ¹²R. G. Fax, M. Hurwitz, and J. R. Melcher, “Dielectrophoretic liquid expulsion.”, Journal of Spacecraft and Rockets **6**, 961–967 (1969).
- ¹³J. E. Boretz, “Orbital refueling techniques”, Journal of Spacecraft and Rockets **7**, 513–522 (1970).
- ¹⁴D. Petrash and R. Raco, “Use of an electric field to attain a zero-gravity liquid-vapor interface configuration under one-gravity”, (1968).

- ¹⁵M. M. Hurwitz, *Dielectrophoretic control of propellant slosh in low gravity final report, 5 jan. 1966 - 31 mar. 1968* (Mar. 31, 1968).
- ¹⁶S. G. P. Berenyi, *Dielectrophoretic baffling to control vapor ingestion in weightlessness* (July 1, 1970).
- ¹⁷I. M. Kirko, E. I. Dobychin, and V. I. Popov, “Phenomenon of the capillary “ball game” under the condition of weightlessness”, Soviet Physics Doklady **15**, 442 (1970).
- ¹⁸A. Wollman, M. Weislogel, B. Wiles, D. Pettit, and T. Snyder, “More investigations in capillary fluidics using a drop tower”, Experiments in Fluids **57**, 57 (2016).
- ¹⁹B. Attari, M. Weislogel, A. Wollman, Y. Chen, and T. Snyder, “Puddle jumping: spontaneous ejection of large liquid droplets from hydrophobic surfaces during drop tower tests”, Physics of Fluids **28**, 102104 (2016).
- ²⁰D. Richard, C. Clanet, and D. Quéré, “Surface phenomena: contact time of a bouncing drop”, Nature **417**, 811 (2002).
- ²¹I. Langmuir, “Surface electrification due to the recession of aqueous solutions from hydrophobic surfaces”, Journal of the American Chemical Society **60**, 1190–1194 (1938).
- ²²K. Yatsuzuka, Y. Mizuno, and K. Asano, “Electrification phenomena of pure water droplets dripping and sliding on a polymer surface”, Journal of Electrostatics **32**, 157–171 (1994).
- ²³J. K. Beattie, “The intrinsic charge on hydrophobic microfluidic substrates”, Lab on a Chip **6**, 1409–1411 (2006).

- ²⁴S. Strazdaite, J. Versluis, and H. J. Bakker, “Water orientation at hydrophobic interfaces”, *The Journal of Chemical Physics* **143**, 084708 (2015).
- ²⁵Pettit Donald, “Flow induced charging of liquids in reduced gravity”, Engineering, Construction, and Operations in Space V, Proceedings 10.1061/40177(207)75.
- ²⁶D. Stevenson, “Electrostatic model applied to ISS charged water droplet experiment”, in (June 16, 2015).
- ²⁷S. A. Czepiela, *The charging of composites in the space environment* (Aug. 1, 1997).
- ²⁸W. Unterberg, “Zero gravity problems in space powerplants: a status survey”, *ARS Journal* **32**, 862–872 (1962).
- ²⁹K. A. White, *Liquid droplet radiator development status* (Jan. 1, 1987).
- ³⁰D. Choi, H. Lee, D. J. Im, I. S. Kang, G. Lim, D. S. Kim, and K. H. Kang, “Spontaneous electrical charging of droplets by conventional pipetting”, *Scientific Reports* **3**, 2037 (2013).
- ³¹F. F. Abraham, “Functional dependence of drag coefficient of a sphere on reynolds number”, *The Physics of Fluids* **13**, 2194–2195 (1970).
- ³²D. A. Saville, “ELECTROHYDRODYNAMICS:the taylor-melcher leaky dielectric model”, *Annual Review of Fluid Mechanics* **29**, 27–64 (1997).
- ³³J. R. Melcher, *Continuum electromechanics / james r. melcher*, Includes index. (MIT Press, Cambridge, Mass).
- ³⁴H. A. Pohl, “Some effects of nonuniform fields on dielectrics”, *Journal of Applied Physics* **29**, 1182–1188 (1958).

- ³⁵X. Wang, X.-B. Wang, and P. R. C. Gascoyne, “General expressions for dielectrophoretic force and electrorotational torque derived using the Maxwell stress tensor method”, *Journal of Electrostatics* **39**, 277–295 (1997).
- ³⁶David J. Griffiths, *Introduction to electrodynamics*, in collab. with Internet Archive (Prentice Hall, 1999), 602 pp.
- ³⁷E. Schmidt, *Droplet-electro-bounce: project files for droplet electro-bounce*, original-date: 2017-06-06T22:20:50Z, June 18, 2017.
- ³⁸*Electrets — gerhard m. sessler — springer ()*.
- ³⁹O. Heaviside, *Electrical papers*, Vol. 2 (Cambridge University Press, 2011).
- ⁴⁰T. Wu, Y. Suzuki, and N. Kasagi, “Low-voltage droplet manipulation using liquid dielectrophoresis on electret”, *Journal of Micromechanics and Microengineering* **20**, 085043 (2010).
- ⁴¹J. Van Turnhout, *Thermally stimulated discharge of polymer electrets: a study on nonisothermal dielectric relaxation phenomena* (Elsevier Science & Technology, 1975).
- ⁴²Y. Wada, H. Oguchi, M. Hara, H. Asanuma, and H. Kuwano, “Stacking electrets for electrostatic vibration energy harvesters”, in Digest tech. PowerMEMS 2012 workshop (2012), pp. 504–507.
- ⁴³H. Ni, R. C. Amme, and Y. Jin, “Desalination by electret technology”, *Desalination* **174**, 237–245 (2005).
- ⁴⁴C. G. L. Furmidge, “Studies at phase interfaces. i. the sliding of liquid drops on solid surfaces and a theory for spray retention”, *Journal of Colloid Science* **17**, 309–324 (1962).

- ⁴⁵D. K. Davies, “The examination of the electrical properties of insulators by surface charge measurement”, *Journal of Scientific Instruments* **44**, 521 (1967).
- ⁴⁶M. M. Perlman, *Electrets, charge storage, and transport in dielectrics*, Vol. 2 (Dielectrics and Insulation Division, Electrochemical Society, 1973).
- ⁴⁷H. T. M. Haenen, “The characteristic decay with time of surface charges on dielectrics”, *Journal of Electrostatics* **1**, 173–185 (1975).
- ⁴⁸G. F. L. Ferreira and M. T. Figueiredo, “Corona charging of electrets: models and results”, *IEEE Transactions on Electrical Insulation* **27**, 719–738 (1992).
- ⁴⁹J. Schindelin, I. Arganda-Carreras, E. Frise, V. Kaynig, M. Longair, T. Pietzsch, S. Preibisch, C. Rueden, S. Saalfeld, B. Schmid, J.-Y. Tinevez, D. J. White, V. Hartenstein, K. Eliceiri, P. Tomancak, and A. Cardona, “Fiji: an open-source platform for biological-image analysis”, *Nature Methods* **9**, 676–682 (2012).
- ⁵⁰C. A. Schneider, W. S. Rasband, and K. W. Eliceiri, “NIH image to ImageJ: 25 years of image analysis”, *Nature Methods* **9**, 671–675 (2012).
- ⁵¹K. Li, *The image stabilizer plugin for ImageJ* (Feb. 2008).
- ⁵²T. E. Oliphant, “Python for scientific computing”, *Computing in Science Engineering* **9**, 10–20 (2007).
- ⁵³A. Savitzky and M. J. E. Golay, “Smoothing and differentiation of data by simplified least squares procedures.”, *Analytical Chemistry* **36**, 1627–1639 (1964).

- ⁵⁴R. W. Schafer, “What is a savitzky-golay filter? [lecture notes]”, IEEE Signal Processing Magazine **28**, 111–117 (2011).
- ⁵⁵A. C. Hindmarsh, “ODEPACK, a systematized collection of ODE solvers, RS stepleman et al.(eds.), north-holland, amsterdam,(vol. 1 of), pp. 55-64.”, IMACS transactions on scientific computation **1**, 55–64 (1983).
- ⁵⁶*Numerical optimization — jorge nocedal — springer ()*.
- ⁵⁷G. A. Wood, “Data smoothing and differentiation procedures in biomechanics”, Exercise and Sport Sciences Reviews **10**, 308 (1982).
- ⁵⁸T. Kolda, R. Lewis, and V. Torczon, “Optimization by direct search: new perspectives on some classical and modern methods”, SIAM Review **45**, 385–482 (2003).
- ⁵⁹J. A. Nelder and R. Mead, “A simplex method for function minimization”, The Computer Journal **7**, 308–313 (1965).
- ⁶⁰C. J. Price, I. D. Coope, and D. Byatt, “A convergent variant of the nelder–mead algorithm”, Journal of Optimization Theory and Applications **113**, 5–19 (2002).
- ⁶¹W. Spendley, G. R. Hext, and F. R. Himsorth, “Sequential application of simplex designs in optimisation and evolutionary operation”, Technometrics **4**, 441–461 (1962).
- ⁶²P. R. Bevington, *Data reduction and error analysis for the physical sciences* (1969).
- ⁶³K. Jaqaman and G. Danuser, “Linking data to models: data regression”, Nature Reviews Molecular Cell Biology **7**, 813 (2006).

⁶⁴T. Takamatsu, Y. Hashimoto, M. Yamaguchi, and T. Katayama, "THEORETICAL AND EXPERIMENTAL STUDIES OF CHARGED DROP FORMATION IN a UNIFORM ELECTRIC FIELD", JOURNAL OF CHEMICAL ENGINEERING OF JAPAN **14**, 178–182 (1981).